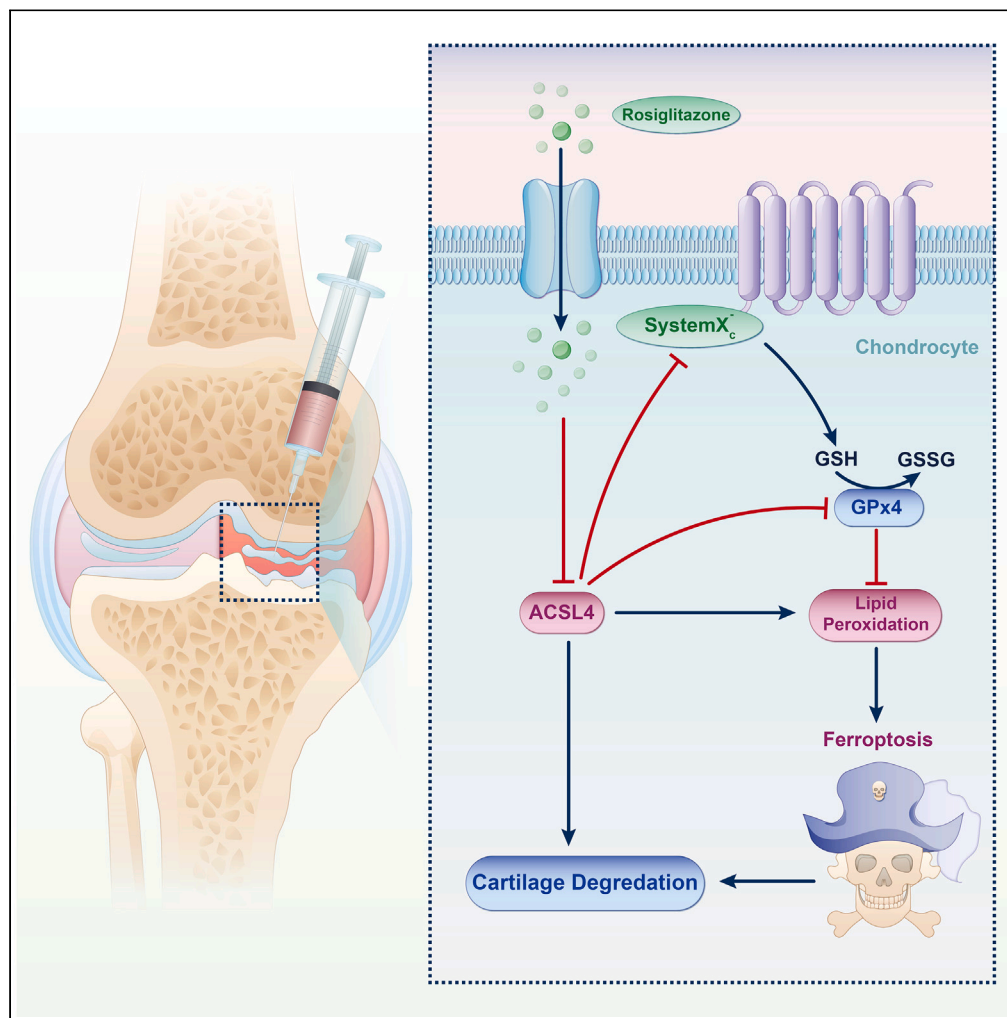**Article**

Rosiglitazone retards the progression of iron overload-induced osteoarthritis by impeding chondrocyte ferroptosis

Siyang Cao, Yihao Wei, Yaohang Yue, ..., Ao Xiong, Peng Liu, Hui Zeng

xiongao@189.cn (A.X.)
liupeng_polymer@126.com (P.L.)
zenghui@pkuszh.com (H.Z.)

Highlights

RSG exhibits anti-ferroptotic effects, mitigating the progression of IOOA

RSG suppresses lipid peroxidation and restores iron homeostasis

RSG is a promising anti-ferroptotic drug candidate for treating IOOA

iScience

Article

Rosiglitazone retards the progression of iron overload-induced osteoarthritis by impeding chondrocyte ferroptosis

Siyang Cao,[1,2,3,5] Yihao Wei,[1,2,3,5] Yaohang Yue,[1,2,3] Yingqi Chen,[1,2,3] Junyu Qian,[1,2,3] Deli Wang,[1,2,3] Ao Xiong,[1,2,3,4,6,*] Peng Liu,[1,2,3,4,6,*] and Hui Zeng[1,2,3,4,6,7,*]

SUMMARY

Ferroptosis is implicated in several diseases, including iron overload-induced osteoarthritis (IOOA), which is marked by oxidative stress, iron imbalance, and lipid peroxidation. Given rosiglitazone's (RSG) ability to inhibit lipid peroxidation and ferroptosis, this study aims to assess its therapeutic potential for treating IOOA. Our *in vitro* results show that RSG targets acyl-CoA synthetase long-chain family member 4 to mitigate impairments induced by interleukin-1 beta and ferric ammonium citrate, including cell apoptosis, senescence, inflammatory responses, extracellular matrix degradation, and ferroptosis. RSG reduced intracellular iron content, alleviated oxidative stress and lipid peroxidation, mitigated damage to membrane-bound organelles, and enhanced glucose transport. Additionally, pre-treatment with RSG imparted anti-ferroptotic properties to chondrocytes. *In vivo*, RSG alleviated cartilage degradation, inflammatory responses, and ferroptosis in mice with IOOA. In conclusion, RSG exhibits chondroprotective and anti-ferroptotic effects by suppressing lipid peroxidation and restoring iron homeostasis, highlighting its potential for treating IOOA.

INTRODUCTION

Osteoarthritis (OA), which affects approximately 7% of the global population, is the most common form of arthritis.[1,2] With the global population aging and obesity rates increasing, the incidence of OA is expected to rise.[3,4] This increase imposes a significant economic and social burden, straining healthcare systems due to costs related to diagnostics, treatment, sick leave, rehabilitation, and early retirement.[5] Since the precise molecular mechanisms underlying OA onset and progression remain poorly understood, current therapies mainly focus on symptom relief.[6]

Traditionally, OA has been attributed to prolonged mechanical stress on the joints.[7] However, advancements in research have revealed the significance of iron homeostasis in arthropathies.[8] Clinical studies have confirmed that OA progression is influenced by the degree of iron overload.[9] Imaging analyses have shown a direct association between OA severity and ferritin levels.[10,11] Weighted median analysis from extensive genome-wide association studies has demonstrated a positive correlation between serum iron, ferritin, transferrin saturation, and OA.[12] These clinical findings suggest a strong link between iron accumulation and the initiation and progression of OA. Cell and animal experiments have elucidated the molecular mechanisms of iron overload, which accelerates OA occurrence and progression.[9,13] Iron overload disrupts cellular iron homeostasis, upsetting the balance between oxidative stress and antioxidant systems. This disruption triggers lipid peroxidation and ferroptosis,[14,15] leading to structural disruption of the extracellular matrix (ECM) and degeneration of articular cartilage.[16–19] Therefore, developing drugs that regulate iron homeostasis, provide antioxidation, and inhibit lipid peroxidation by suppressing ferroptosis may offer a novel strategy for OA treatment. Currently, research on iron overload-induced OA (IOOA) focuses on regulating the two primary components of ferroptosis (redox and iron homeostasis),[20–23] with limited attention to the proximate executioners of ferroptosis—lipid peroxidation.[19]

Essential substrates susceptible to ferroptotic lipid peroxidation include phospholipids with polyunsaturated fatty acid (PUFA) chains.[24] Free PUFAs have a notable affinity for membrane phospholipids. Acyl-CoA synthetase long-chain family member 4 (ACSL4) plays a crucial

[1]National & Local Joint Engineering Research Center of Orthopaedic Biomaterials, Peking University Shenzhen Hospital, Shenzhen, Guangdong 518036, People's Republic of China
[2]Shenzhen Key Laboratory of Orthopaedic Diseases and Biomaterials Research, Peking University Shenzhen Hospital, Shenzhen, Guangdong 518036, People's Republic of China
[3]Department of Bone & Joint Surgery, Peking University Shenzhen Hospital, Shenzhen, Guangdong 518036, People's Republic of China
[4]Present address: No. 1120 Lianhua Road, Futian District, Shenzhen, Guangdong Province, People's Republic of China
[5]These authors contributed equally
[6]These authors contributed equally
[7]Lead contact
*Correspondence: xiongao@189.cn (A.X.), liupeng_polymer@126.com (P.L.), zenghui@pkuszh.com (H.Z.)
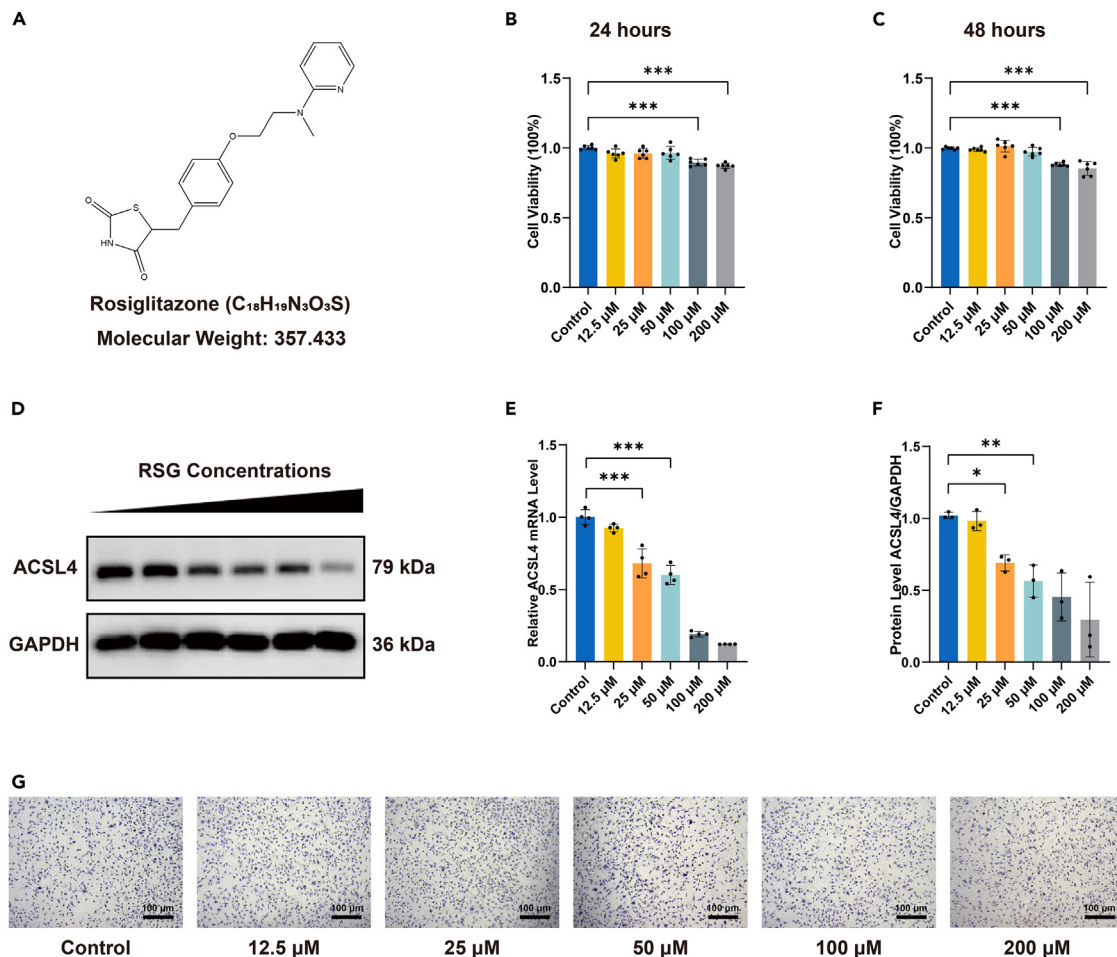https://doi.org/10.1016/j.isci.2024.110526

Figure 1. Effect of different concentrations of RSG on chondrocytes

(A) Structural formula of RSG (molecular formula: $C_{18}H_{19}N_3O_3S$; molecular weight: 357.43).

(B and C) Chondrocytes were treated with varying concentrations of RSG (0, 12.5, 25, 50, 100, 200 μM) for 24 and 48 h (n = 6 per group).

(D) Levels of ACSL4 in chondrocytes after stimulation with different concentrations of RSG for 24 h were measured by Western Blot.

(E) Variation in *ACSL4* mRNA expression levels with different concentrations of RSG (n = 4 per group).

(F) Protein expression levels of ACSL4 in chondrocytes treated with varying concentrations of RSG (n = 3 per group).

(G) Chondrocyte morphology revealed by toluidine blue staining (scale bar = 100 μm). Two-tailed p values were calculated, and statistical significance was defined as $p < 0.05$, denoted as 'ns' for no statistical difference, and indicated as *$p < 0.05$, **$p < 0.01$, ***$p < 0.001$. All experiments and images shown are representative.

role in the thioesterification of PUFAs by forming acyl-CoA derivatives through interaction with coenzyme A during phospholipid metabolism. Therefore, hindering the generation of phospholipid-PUFA by decreasing ACSL4 expression prevents ferroptosis.[25–27] The widely used thiazolidinedione, rosiglitazone (RSG), can suppress ACSL4 activity, inhibiting lipid peroxidation and ferroptosis in smooth muscle and lung epithelial cells.[28–31] Therefore, RSG may be used in clinical interventions of IOOA.[9,19]

In this study, we simulated inflammatory conditions and induced iron overload *in vitro* using interleukin-1 beta (IL-1β) and ferric ammonium citrate (FAC), respectively. Furthermore, destabilized medial meniscus (DMM) surgery and iron dextran (ID) administration were used to induce IOOA *in vivo*. We hypothesized that RSG can mitigate cartilage degeneration and slow IOOA progression by inhibiting chondrocyte ferroptosis, making it a potential therapeutic candidate.

RESULTS

Effect of different concentrations of RSG on chondrocytes

The chemical structure of RSG is shown in Figure 1A. Cytotoxicity of various RSG concentrations on chondrocytes was assessed at 24 and 48 h (Figures 1B and 1C). RSG treatments (100 and 200 μM) for 24 and 48 h significantly suppressed chondrocyte viability ($p < 0.05$), while concentrations from 0 to 50 μM showed no significant cytotoxicity. As RSG is an ACSL4 inhibitor, its effect on ACSL4 mRNA expression and protein
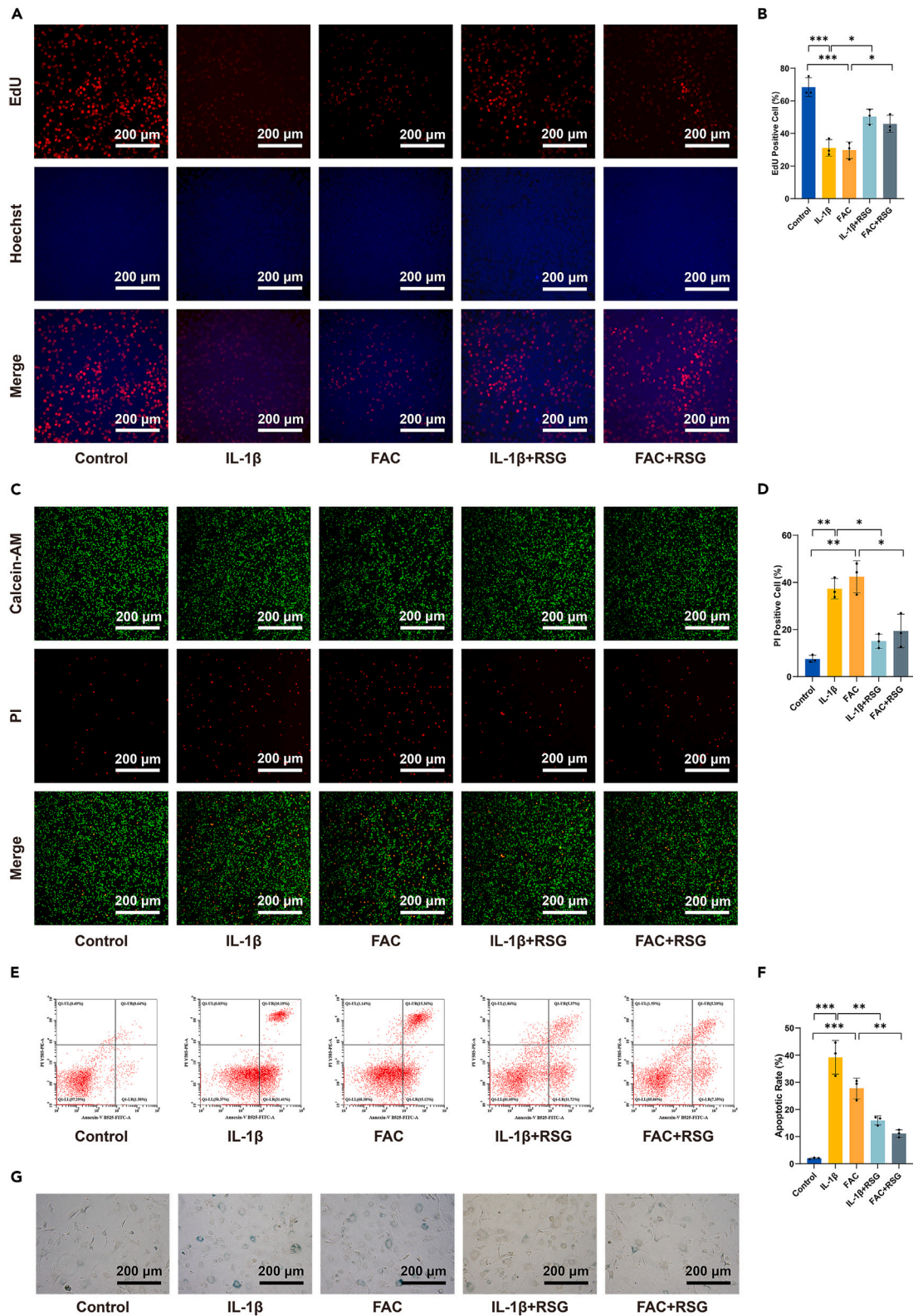
Figure 2. RSG protects chondrocytes from IL-1β/FAC-induced proliferation inhibition, cell death, and senescence

(A) Cell proliferation determined by EdU staining (scale bar = 200 μm).

(B) Semi-quantitative results of EdU staining fluorescence intensity (n = 3 per group).

(C) The cell viability was determined by the Calcein-AM/PI live-dead staining (scale bar = 200 μm).

(D) Semi-quantitative results of the PI staining assay (n = 3 per group).

(E) Apoptosis assessed using Annexin V-FITC/PI staining.

(F) Quantitative analysis of the apoptotic rate (n = 3 per group).

(G) Senescence scored by β-galactosidase staining (scale bar = 200 μm). Two-tailed p values were calculated, and statistical significance was defined as $p < 0.05$, denoted as 'ns' for no statistical difference, and indicated as *$p < 0.05$, **$p < 0.01$, ***$p < 0.001$. All experiments and images shown are representative.

levels was examined at different concentrations (Figures 1D–1F). Increasing concentrations of RSG significantly decreased ACSL4 mRNA and protein levels ($p < 0.05$). Chondrocyte morphology was assessed with toluidine blue (TB) staining. A slight decrease in color intensity was observed in chondrocytes treated with 100 and 200 μM RSG compared to the control group (Figure 1G). Based on these results, 50 μM RSG was selected for subsequent *in vitro* experiments.

RSG protects chondrocytes from IL-1β/FAC-induced proliferation inhibition, cell death, and senescence

The 5-Ethynyl-2′-Deoxyuridine (EdU) assay (Figures 2A and 2B) confirmed that both IL-1β and FAC significantly suppressed chondrocyte proliferation. However, RSG partially restored the proliferative ability of cells inhibited by IL-1β/FAC ($p < 0.05$), indicating a protective effect on chondrocytes. This result was further validated by Calcein-AM/propidium iodide (PI) double staining ($p < 0.05$) (Figures 2C and 2D). The protective potential of RSG against IL-1β/FAC-induced apoptosis in chondrocytes was assessed using Annexin V-FITC/PI staining. Apoptosis induction was significantly higher in both IL-1β and FAC-treated groups compared to the control group ($p < 0.05$) (Figures 2E and 2F). Conversely, RSG treatment exhibited a protective effect, mitigating the apoptotic impact of inflammation or iron overload in chondrocytes. Cell senescence was assessed using β-galactosidase staining. IL-1β and FAC accelerated cellular senescence, evidenced by a blue appearance in aging chondrocytes. Notably, RSG partially alleviated this effect (Figure 2G). These results demonstrate that RSG protects chondrocytes from IL-1β/FAC-induced proliferation inhibition, cell death, and senescence.

RSG mitigates IL-1β/FAC-induced inflammation, ECM degradation, and ferroptosis in chondrocytes

As an *in vitro* model for OA, IL-1β is commonly used to induce inflammation in chondrocytes, while FAC is utilized to establish an iron overload cell model.[20,23,32,33] In this study, the model groups (IL-1β and FAC) exhibited significantly increased expression levels of proinflammatory cytokines (Tumor Necrosis Factor-alpha (TNF-α), cyclooxygenase-2 (COX-2), nitric oxide synthase 2 (iNOS), and interleukin-6 (IL-6)), whereas RSG markedly reduced these proinflammatory cytokines ($p < 0.05$) (Figures 3A and 3D–3G). Among the matrix-degrading enzymes, matrix metallopeptidase 3 (MMP3), matrix metallopeptidase 13 (MMP13), and ADAM metallopeptidase with thrombospondin type 1 motif 5 (ADAMTS5) play crucial roles in the destruction of OA cartilage.[34,35] qPCR and Western Blot results in this experiment indicated that both IL-1β and FAC could promote cartilage catabolism, while RSG significantly suppressed this effect ($p < 0.05$) (Figures 3A and 3I–3J).

Several markers, such as glutathione peroxidase (GPx4), solute carrier family 7 member 11 (SLC7A11), and regulator of G protein signaling 4 (RGS4), are downregulated during ferroptosis, while ACSL4, transferrin receptor 1 (TfR1), and ChaC glutathione-specific gamma-glutamyl-cyclotransferase 1 (CHAC1) are induced; altered expression of these markers serves as indicators of ferroptosis.[36] Under conditions of inflammation or iron overload, there was a notable reduction in the mRNA and protein expression of GPx4, SLC7A11, and RGS4, whereas ACSL4, TfR1, and CHAC1 exhibited a substantial increase (Figures 3B, 3C and 3H–3K) ($p < 0.05$). These findings suggest that both IL-1β and FAC induce ferroptosis in chondrocytes. The expression of ACSL4, TfR1, and CHAC1 was significantly inhibited by RSG, while the expression of GPx4, SLC7A11, and RGS4 in chondrocytes was concurrently enhanced, highlighting its anti-ferroptotic efficacy (Figures 3B, 3C, and 3H–3K) ($p < 0.05$). These results demonstrate the ability of RSG to alleviate IL-1β/FAC-induced inflammatory responses, ECM degradation, and ferroptosis in chondrocytes.

RSG decreases IL-1β/FAC-induced intracellular iron content and oxidative stress levels

Given the involvement of cellular Fe^{2+} accumulation in ferroptosis, this study analyzed Fe^{2+} levels.[37] Initially, chondrocytes were stained with the probe FerroOrange, which selectively reacts with Fe^{2+} rather than Fe^{3+}. The signal intensity of FerroOrange markedly increased with the concentration of Fe^{2+} in IL-1β/FAC-treated cells, while RSG treatment significantly reduced Fe^{2+} levels under IL-1β/FAC treatment (Figures 4A, 4B, 4E, and 4F) ($p < 0.05$). Similarly, Mito-FerroGreen staining revealed a substantial increase in the fluorescence intensity of chondrocytes upon IL-1β/FAC treatment, indicating elevated levels of mitochondrial Fe^{2+}, whereas RSG treatment reversed iron accumulation (Figures 4C, 4D, 4G, and 4H) ($p < 0.05$). Furthermore, the ferrous ion content assay kit also validated these results (Figure 4I) ($p < 0.05$). These observations suggest that RSG could rescue IL-1β/FAC-induced iron metabolic disorders *in vitro*.

Apart from disruptions in iron metabolism, dysregulation of reactive oxygen species (ROS) homeostasis is another hallmark of ferroptosis.[9,38–40] In this experiment, intracellular oxidative stress levels within mitochondria were assessed using the mtSOX Deep Red probe. IL-1β/FAC-induced oxidative stress led to mitochondrial ROS release, evidenced by an increase in mtSOX Deep Red intensity following IL-1β/FAC treatment (Figures 4J and 4K) ($p < 0.05$). However, mitochondrial ROS levels in chondrocytes decreased after RSG treatment (Figures 4J and 4K) ($p < 0.05$). Additionally, the DCFH-DA fluorescent probe was utilized to detect intracellular ROS levels. It was observed
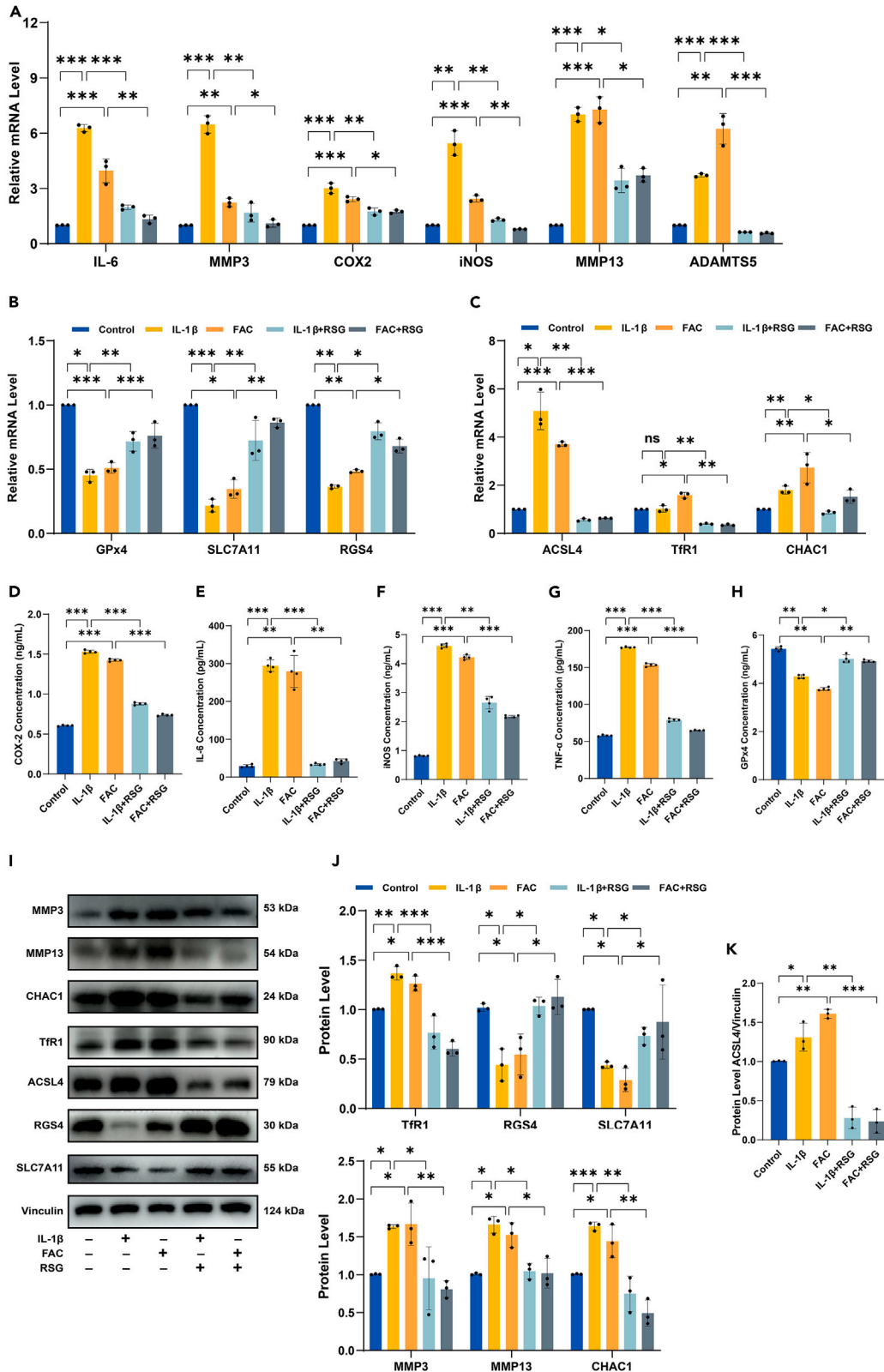
Figure 3. RSG mitigates IL-1β/FAC-induced inflammation, ECM degradation, and ferroptosis in chondrocytes

(A) Relative mRNA expression levels of proinflammatory cytokines (*IL-6, COX-2,* and *iNOS*) and genes related to ECM degradation (*MMP3, MMP13,* and *ADAMTS5*) (*n* = 3 per group).

(B and C) Relative mRNA expression levels of ferroptosis-related genes (*GPx4, SLC7A11, RGS4, ACSL4, TfR1,* and *CHAC1*) (*n* = 3 per group).

(D–G) ELISA applied to detect levels of proinflammatory cytokines (COX-2, IL-6, iNOS, and TNF-α) (*n* = 4 per group).

(H) GPx4 protein levels detected with ELISA (*n* = 4 per group).

(I) Protein expression levels of MMP3, MMP13, CHAC1, TfR1, ACSL4, RGS4, and SLC7A11 detected by Western Blot.

(J and K) Expression quantified by densitometry of bands and reported relative to Vinculin (*n* = 3 per group). Two-tailed *p* values were calculated, and statistical significance was defined as *p* < 0.05, denoted as 'ns' for no statistical difference, and indicated as **p* < 0.05, ***p* < 0.01, ****p* < 0.001. All experiments and images shown are representative.

that IL-1β/FAC induced an increase in ROS in chondrocytes, which significantly reduced after treatment with RSG (Figures 4L–4O) (*p* < 0.05). Considering that glutamate and glutamine contribute to the production of glutathione (GSH) and nicotinamide adenine dinucleotide phosphate, intracellular ROS levels can be inferred by measuring glutamate and glutamine concentrations. Lower glutamine levels correspond to higher ROS levels, while higher glutamate levels indicate lower ROS levels.[41] Analysis of glutamine and glutamate content in each experimental group shows a consistent trend: both IL-1β and FAC increase intracellular glutamate levels while decreasing glutamine levels in chondrocytes (Figures 4P and 4Q) (*p* < 0.05). RSG treatment reversed these results (Figures 4P and 4Q) (*p* < 0.05). Furthermore, reduced GSH, oxidized glutathione (GSSG), and the GSH/GSSG ratio were assessed. The IL-1β and FAC group exhibited a significant decrease in both GSH and the GSH/GSSG ratio, while GSSG levels were notably elevated compared to the control group (Figures 4R–4T) (*p* < 0.05). In the rescue experiments, RSG reversed the decline of GSH and the GSH/GSSG ratio while increasing GSSG levels (*p* < 0.05). In addition to the primary findings, an assessment of superoxide dismutase (SOD) activity in various treatment groups was conducted. The results align with other *in vitro* antioxidant tests, confirming the remarkable antioxidant efficacy of RSG (Figure 4U) (*p* < 0.05).

RSG reduces the levels of lipid peroxidation within chondrocytes initiated by IL-1β/FAC

Ferroptosis is characterized by the excessive accumulation of membrane lipid peroxides.[27] The presence of inflammatory mediators and iron overload exacerbates lipid peroxidation within chondrocytes, potentially contributing to ferroptosis and the pathogenesis of the condition.[42] In this study, intracellular lipid peroxides were assessed using various methods. Liperfluo fluorescence analysis revealed a significant increase in lipid peroxidation in response to IL-1β/FAC stimulation, which was mitigated by RSG (Figures 5A, 5B, 5G, and 5H) (*p* < 0.05). Malondialdehyde (MDA) and 4-hydroxynonenal (4-HNE), recognized as primary biomarkers for lipid peroxidation, are also implicated in various pathological processes associated with OA development.[42] IL-1β/FAC exposure elevated MDA and 4-HNE levels in chondrocytes, an effect significantly attenuated by RSG treatment (Figures 5C and 5F) (*p* < 0.05). Similarly, results from C11 BODIPY[581/591] fluorescent probes corroborated these findings, with RSG mitigating intracellular lipid peroxidation levels (Figures 5D, 5E, 5I, and 5J) (*p* < 0.05). These results highlight the potential of RSG as a therapeutic agent targeting lipid peroxidation in cell-based therapy.

RSG alleviates IL-1β/FAC-induced damage to membrane-containing organelles

During ferroptosis, cellular structural changes such as mitochondrial atrophy and alterations in mitochondrial cristae structure are observed, distinguishing it from other forms of cell death.[36,43] To investigate the impact of IL-1β/FAC on mitochondria *in vitro* and evaluate the potential protective effects of RSG on mitochondrial ultrastructure changes, transmission electron microscopy was employed to examine mitochondrial ultrastructure. As shown in Figure 6A, IL-1β/FAC induced alterations in mitochondrial structure indicative of ferroptosis, which were significantly attenuated by RSG treatment. Besides morphological changes, ferroptosis is associated with abnormal mitochondrial membrane potential (ΔΨm).[44,45] Reduced fluorescent intensity following Rhodamine 123 staining indicated impaired ΔΨm due to IL-1β/FAC treatment, partially restored by RSG administration (Figures 6B~6D) (*p* < 0.05). This result was further confirmed by JC-1 staining (Figures S1G and S1H) (*p* < 0.05).

Lipid peroxidation can damage organelle membranes, including those of mitochondria, endoplasmic reticulum (ER), lysosomes, and the Golgi apparatus, during ferroptosis.[24,46,47] In this study, the LysoTracker red (LTR), Mito-Tracker Green (MTG), ER-Tracker Green (ETG), and Golgi-Tracker Red (GTR) kits were employed to assess lysosomal, mitochondrial, ER, and Golgi apparatus mass, respectively. Chondrocytes treated with IL-1β/FAC exhibited a reduction in lysosomal, mitochondrial, ER, and Golgi apparatus mass (Figures 6E–6I and S1A–S1F) (*p* < 0.05). However, RSG mitigated the IL-1β/FAC-induced loss of organelle mass to some extent (Figures 6E–6I and S1A–S1F) (*p* < 0.05). These findings suggest that RSG can ameliorate damage to membrane-containing organelles caused by lipid peroxidation, highlighting its potential as an anti-ferroptotic agent.

RSG preconditioning confers anti-ferroptotic property upon chondrocytes

Chondrocytes were pretreated with or without 50 μM RSG for 24 h before being stimulated with different concentrations (0.1/1/5 μM) of Erastin, a classical ferroptosis inducer, for an additional 24 h to validate whether RSG could confer anti-ferroptotic properties to chondrocytes. Immunofluorescence staining was subsequently applied to detect the expression levels of three critical proteins (ACSL4, GPx4, and TfR1) involved in ferroptosis. Erastin upregulated the protein levels of ACSL4 and TfR1 and significantly decreased the protein level of GPx4 within chondrocytes (Figures 7A–7C and 7E–7G) (*p* < 0.05). In RSG-preconditioned chondrocytes, similar trends of changes were observed in the
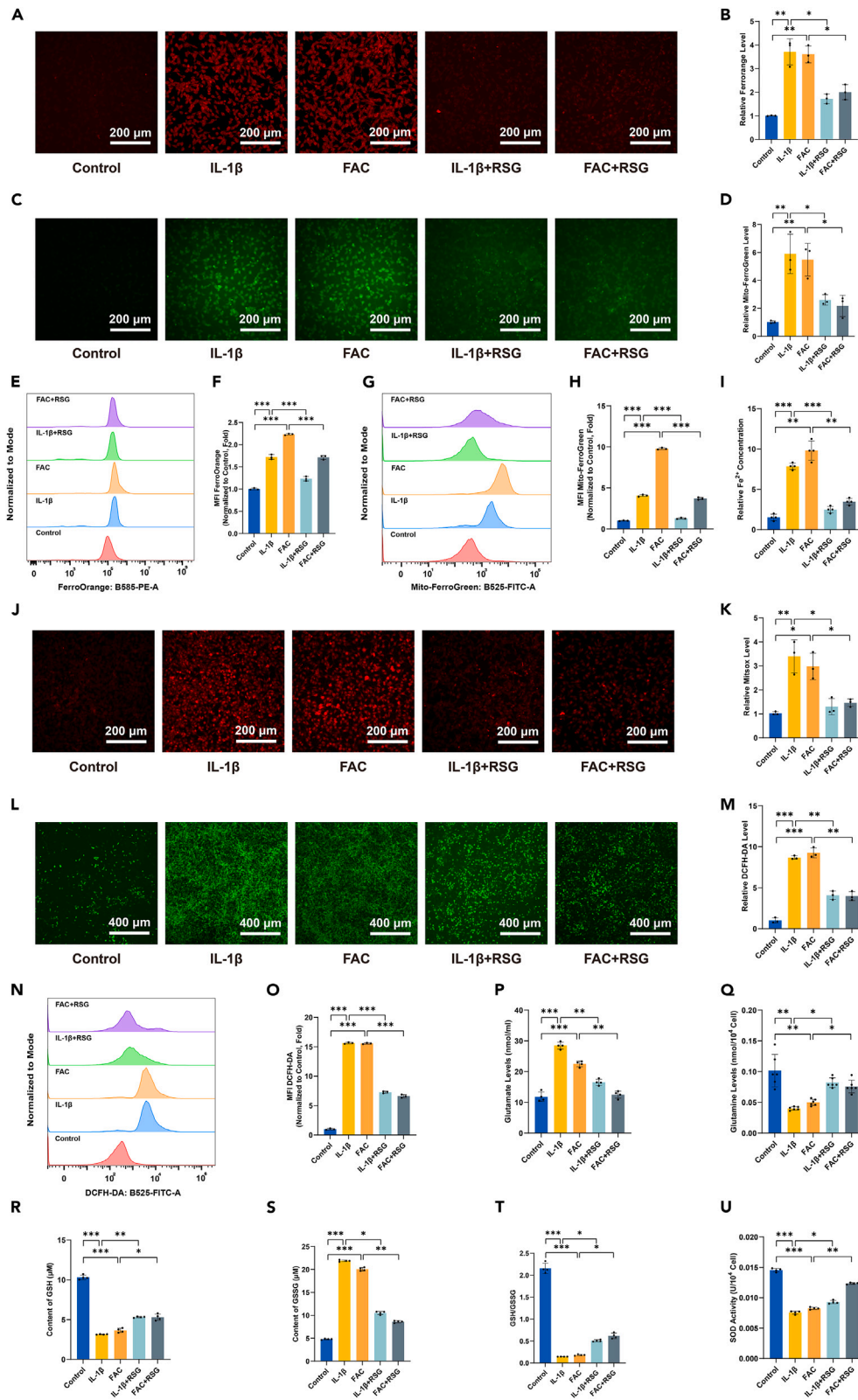
Figure 4. RSG decreases IL-1β/FAC-induced intracellular iron content and oxidative stress levels

(A) Intracellular Fe^{2+} detected by FerroOrange and visualized using fluorescence microscopy (scale bar = 200 μm).

(B) Quantification of FerroOrange fluorescence intensity (n = 3 per group).

(C) Mitochondrial Fe^{2+} concentration determined via Mito-FerroGreen and visualized using fluorescence microscopy (scale bar = 200 μm).

(D) Quantification of Mito-FerroGreen fluorescence intensity (n = 3 per group).

(E) Intracellular Fe^{2+} detected by flow cytometry using FerroOrange.

(F) Quantitative analysis of flow cytometric measurements (n = 3 per group).

(G) Intramitochondrial Fe^{2+} concentration detected by flow cytometry using Mito-FerroGreen.

(H) Quantitative analysis of flow cytometry (n = 3 per group).

(I) Levels of Fe^{2+} in chondrocytes detected using a Fe^{2+} content assay kit (n = 4 per group).

(J) Mitochondrial oxidative stress levels evaluated by mtSOX Deep Red and visualized using fluorescence microscopy (scale bar = 200 μm).

(K) Quantification of mtSOX Deep Red fluorescence intensity (n = 3 per group).

(L) Intracellular ROS detected by DCFH-DA and visualized using fluorescence microscopy (scale bar = 400 μm).

(M) DCFH-DA fluorescence intensity quantification (n = 3 per group).

(N) Fluorescence intensity of DCFH-DA detected using flow cytometry.

(O) Quantitative analysis of flow cytometry (n = 3 per group).

(P and Q) Levels of glutamate (n = 4 per group) and glutamine (n = 6 per group).

(R) Intracellular GSH content (n = 4 per group).

(S) Intracellular GSSG content (n = 4 per group).

(T) Intracellular GSH/GSSG (glutathione redox ratio) (n = 4 per group).

(U) Intracellular SOD activity measurement (n = 4 per group). Two-tailed p values were calculated, and statistical significance was defined as $p < 0.05$, denoted as 'ns' for no statistical difference, and indicated as $*p < 0.05$, $**p < 0.01$, $***p < 0.001$. All experiments and images shown are representative.

expression of all three proteins, albeit with a relatively smaller magnitude of change (Figures 7A–7C and 7E–7G) ($p < 0.05$). Additionally, the expression levels of ACSL4 and TfR1 followed a concentration-dependent downregulation trend with decreasing Erastin concentrations, while GPx4 exhibited the opposite trend (Figures 7A–7C and 7E–7G) ($p < 0.05$). Similar experiments were conducted using FAC. Chondrocytes were pretreated with or without 50 μM RSG for 24 h before being stimulated with different concentrations (100/200/400 μM) of FAC. Intracellular iron deposits were detected by Prussian blue iron staining. The results revealed that iron content increased after FAC treatment, while RSG-preconditioned chondrocytes exhibited resistance to intracellular iron accumulation to some extent (Figure 7D). These experiments demonstrate that RSG pretreatment indeed confers anti-ferroptotic capability to chondrocytes.

RSG enhances glucose transport in chondrocytes

We first examined the effect of varying RSG concentrations on intracellular glucose content. As RSG concentration increased (≥ 50 μM), intracellular glucose content also increased (Figure S2A, $p < 0.05$). Given that chondrocyte glucose transport mainly depends on glucose transporter type 1 (GLUT1),[48] we analyzed GLUT1 expression levels *in vitro*. The results confirmed that RSG enhances glucose transport by upregulating GLUT1 expression, thereby increasing intracellular glucose content in chondrocytes (Figures S2B and S2C, $p < 0.05$). IL-1β treatment decreased intracellular glucose content in chondrocytes, while RSG increased it (Figure S2D, $p < 0.05$). Consistent with previous research,[49–51] our Western Blot analysis showed that IL-1β accelerates glucose transport by upregulating GLUT1 in chondrocytes (Figures S2E and S2F, $p < 0.05$). This upregulation appears to be an important component of the chondrocytes' inflammatory response. Furthermore, RSG increased GLUT1 expression, mitigating the disrupted glucose metabolism caused by IL-1β (Figures S2E and S2F, $p < 0.05$). The results of the above experiments suggest that RSG enhances glucose transport within chondrocytes.

RSG enhances the protective effect of ACSL4 knockdown in IL-1β-treated chondrocytes

To investigate further, we knocked down ACSL4 using small interfering RNA (siRNA). The results indicated that silencing ACSL4 (si-ACSL4) ameliorated the levels of aberrant key proteins involved in ferroptosis (ACSL4, LPCAT3, and SLC7A11), inflammatory responses (COX-2), and ECM degradation (MMP3 and MMP13) under IL-1β stimulation (Figures S3 and S4, $p < 0.05$). Based on ACSL4 knockdown, the application of RSG further enhanced the suppression of ACSL4 and ECM degradation and improved anti-ferroptotic effects (Figure S4, $p < 0.05$). Molecular docking further confirmed the interaction between RSG and ACSL4 (Figure S5). Multiple residues formed interactions between the receptor protein and the ligand. These interactions resulted in a binding energy of −8.5 kcal/mol, indicating strong binding affinity.

RSG attenuates cartilage degeneration *in vivo*

Since both IL-1β (associated with inflammation) and FAC (related to iron overload) induced ferroptosis in chondrocytes *in vitro*, we further investigated whether RSG could mitigate the progression of OA/IOOA *in vivo*. The OA/IOOA mouse model was established using DMM surgery and periodic intraperitoneal injections of ID (Figure 8A). Throughout the experimental period, no animals succumbed to accidents or other unexpected causes, and no infections or inflammations were observed at the surgical sites. The safety profile of RSG local injection into the joint cavity appears promising, as evidenced by the steady increase in body weight of mice in each administration group, and no significant differences were observed in blood routine indices, serum glucose, hepatic function, and renal function across the various groups
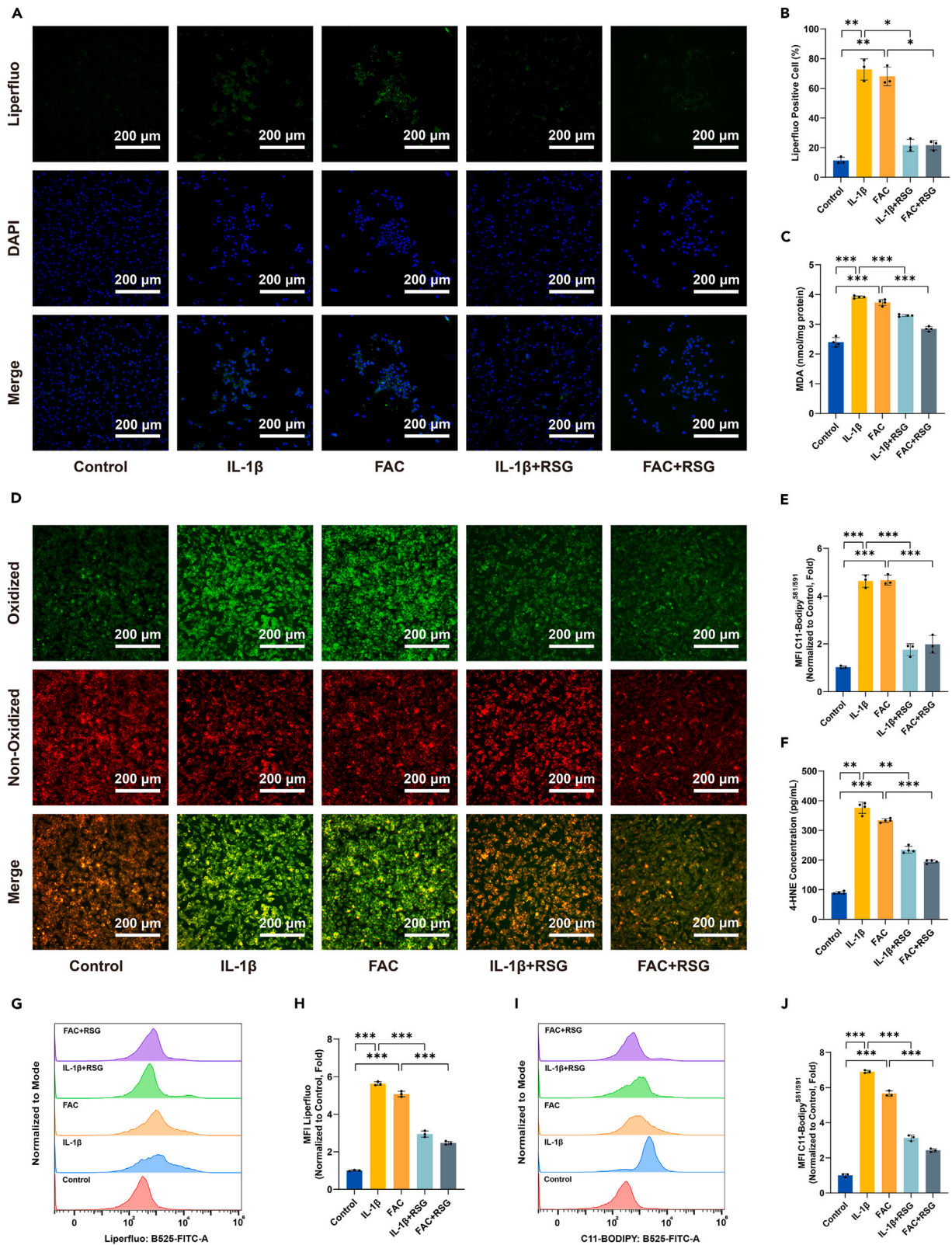
Figure 5. RSG reduces the levels of lipid peroxidation within chondrocytes initiated by IL-1β/FAC

(A) Lipid peroxides in chondrocytes under different treatments detected by Liperfluo probes (scale bar = 200 μm).

(B) Quantification of Liperfluo fluorescence (n = 3 per group).

(C) The MDA contents were determined by the lipid peroxidation MDA assay kit (n = 4 per group).

(D) Detection of lipid peroxidation by C11 BODIPY$^{581/591}$ fluorescent probe (scale bar = 200 μm).

(E) Quantification of C11 BODIPY$^{581/591}$ fluorescence (n = 3 per group).

(F) 4-HNE levels in the chondrocytes determined by ELISA (n = 4 per group).

(G) Fluorescence intensity of Liperfluo detected using flow cytometry.

(H) Quantitative analysis of flow cytometric measurements (n = 3 per group).

(I) Fluorescence intensity of C11 BODIPY$^{581/591}$ detected using flow cytometry.

(J) Quantitative analysis of flow cytometric measurements (n = 3 per group). Two-tailed p values were calculated, and statistical significance was defined as $p < 0.05$, denoted as 'ns' for no statistical difference, and indicated as *$p < 0.05$, **$p < 0.01$, ***$p < 0.001$. All experiments and images shown are representative.

(Figures S6A–S6J) ($p > 0.05$). Furthermore, historical evaluations showed no significant differences in major organs among all groups (Figure S6K) ($p > 0.05$).

Micro-computed tomography (micro-CT) analysis revealed a significant increase in osteophyte formation, including osteophyte size and maturity, 8 weeks after DMM surgery (Figures 8B, 8D, and 8E) ($p < 0.05$). Additionally, IOOA further exacerbated this trend. Treatment with RSG restrained osteophyte formation (Figures 8B, 8D, and 8E) ($p < 0.05$). For a comprehensive assessment of articular cartilage damage in the knee joint among groups, histological analyses, including staining with Hematoxylin-Eosin (H&E), Saffron-O and Fast Green (SOFG), and TB, were conducted. In the histopathological examination of the DMM group, progressive degeneration of articular cartilage was evident, leading to decreased cartilage thickness and increased roughness of the articular surface (Figures 8C and 8H) ($p < 0.05$). Mice in the IOOA group exhibited thinner articular cartilage, more severe cartilage erosion, cartilage matrix loss, and uneven distribution of chondrocytes compared to other groups (Figures 8C and 8H) ($p < 0.05$). Conversely, RSG treatment suppressed cartilage thickness loss and alleviated chondrocyte disorganization in mice knee joints to a certain extent (Figures 8C and 8H) ($p < 0.05$). The modified Mankin and Osteoarthritis Research Society International (OARSI) scores suggested that intra-articular injection of RSG ameliorated the severity of articular cartilage destruction with statistical significance (Figures 8F and 8G) ($p < 0.05$). These findings indicate that RSG can decelerate the deterioration of articular cartilage degeneration in the mice OA/IOOA model.

RSG alleviated chondrocyte inflammatory responses, ECM degradation, and ferroptosis within the surgery-induced mouse OA model

To further investigate the impact of RSG on ferroptosis in chondrocytes within the OA/IOOA mouse model, immunohistochemical (IHC) analysis was conducted. The IHC analysis revealed a significant upregulation in the expression of ADAMTS5, MMP3, and COX-2 in both the DMM and IOOA groups (Figure 9) ($p < 0.05$). Notably, our investigation also showed an elevation in the levels of ferroptosis-related markers, such as 4-HNE, ACSL4, and TfR1, coupled with a reduction in the expression of GPx4 and nuclear factor erythroid 2-related factor 2 (Nrf2) in the DMM and IOOA groups compared to the Sham group (Figure 9) ($p < 0.05$). It is crucial to emphasize that the sensitivity to ferroptosis is intricately connected to the expression levels of Nrf2.[52] An upregulation in Nrf2 expression inhibits ferroptosis, while a downregulation fosters the occurrence of ferroptosis.

Notably, these changes were more pronounced in the IOOA group than in the DMM group. Treatment with varying concentrations of RSG partially alleviated these alterations (Figure 9) ($p < 0.05$). Collectively, these *in vivo* findings strongly support the notion that RSG can attenuate cartilage degradation, chondrocyte inflammatory responses, and ferroptosis, thereby impeding the progression of OA/IOOA in the mouse model. These results align with the observations made in our *in vitro* experiments.

DISCUSSION

As the most abundant essential metal in mammals, iron plays a pivotal role in diverse biological reactions within living organisms.[9] However, an excess of ions can over-trigger the iron-dependent Fenton reaction, generating large amounts of ROS and eventually inducing membrane lipid peroxidation. This process may lead to ferroptosis and various diseases associated with oxidative stress, iron dysregulation, or lipid peroxidation.[42,53] Currently, in the research domain of IOOA, the emphasis is on oxidative stress and iron homeostasis. A key area of investigation should focus on enhancing chondrocyte resistance to lipid peroxidation induced by iron overload.[19] Researchers have demonstrated that pharmacological inhibition of ACSL4 represents a feasible therapeutic strategy to impede the execution of ferroptosis by suppressing lipid peroxidation.[54–56] Among the candidate drugs, RSG stands out as the most potent specific inhibitor of ACSL4, exhibiting a comparable effect to ACSL4 knockout.[57–59] This inhibition results in a notable decrease in MDA, a substantial reduction in iron accumulation, diminished levels of proinflammatory cytokines, heightened antioxidant levels, and holds promise for the prevention and treatment of diverse conditions, such as acute kidney injury, ischemia/reperfusion injury, and surgical brain injury.[28,58,60–71] In this study, we posit that the progression of IOOA can be impeded by RSG due to its anti-ferroptotic effects, specifically targeting ACSL4.

In the *in vitro* investigation, an inflammatory environment and iron overload were induced in chondrocyte cultures by adding IL-1β and FAC to the media. Consistent with previous findings,[20–23,32,33,72] various experiments, including flow cytometry and fluorescence assays, revealed that treatment with IL-1β/FAC significantly promoted ECM degradation, inhibited cell proliferation, increased iron/ROS/lipid ROS levels, enhanced cellular senescence, reduced ΔΨm, and damaged major membrane-containing organelles, primarily mitochondria. These changes
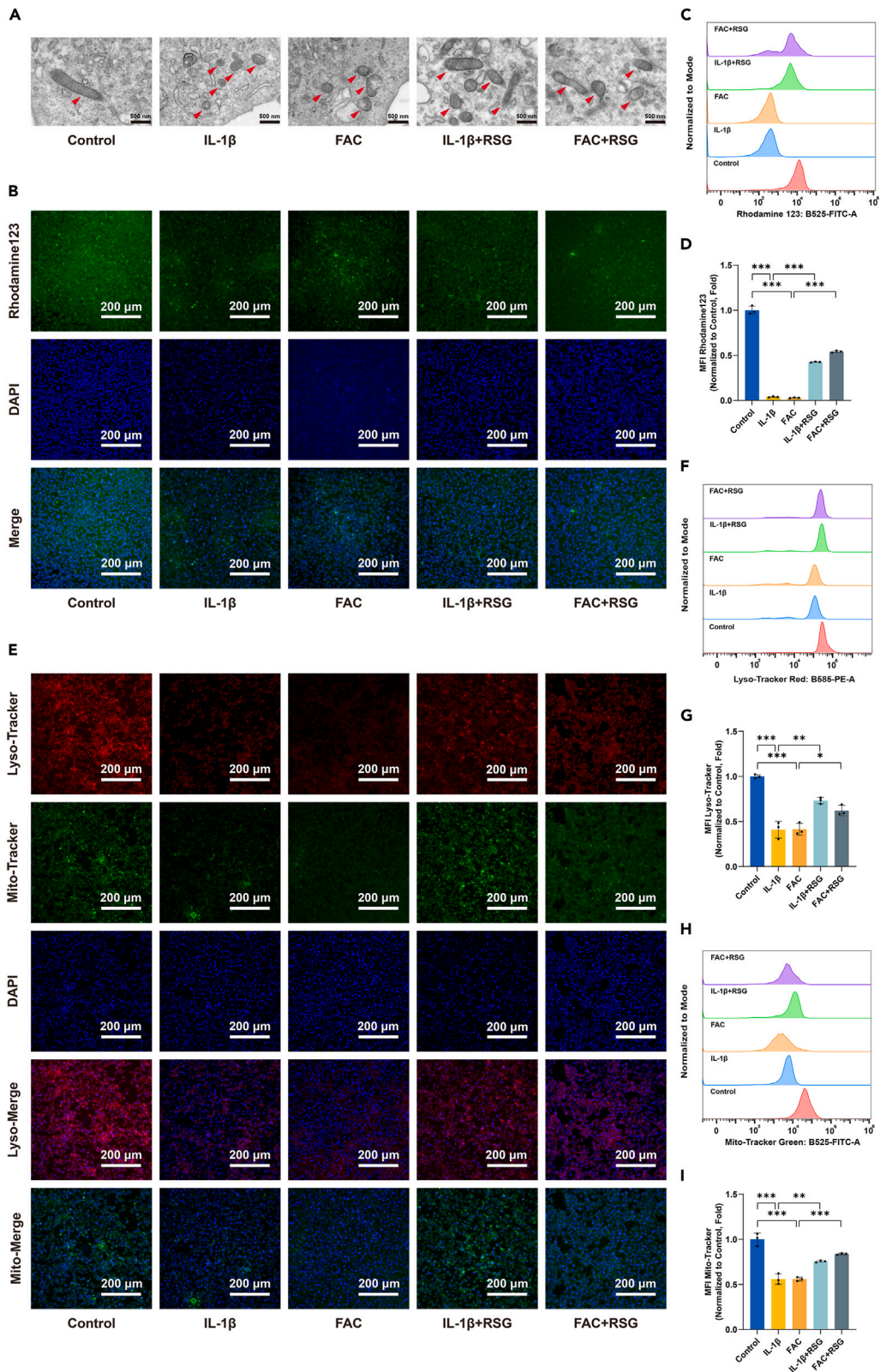
Figure 6. RSG alleviates IL-1β/FAC-induced injury to mitochondria and lysosomes

(A) Mitochondria in chondrocytes were visualized by transmission electron microscopy, with red arrows indicating the location of mitochondria (scale bar = 500 nm).

(B) Detection of the changes in mitochondrial membrane potential using Rhodamine 123 (scale bar = 200 μm).

(C) Fluorescence intensity of Rhodamine 123 detected using flow cytometry.

(D) Quantitative analysis of flow cytometric measurements (*n* = 3 per group).

(E) Lysosomal and mitochondrial mass were evaluated by LysoTracker red and Mito-Tracker Green staining respectively (scale bar = 200 μm).

(F) Fluorescence intensity of LysoTracker red detected using flow cytometry.

(G) Quantitative analysis of flow cytometric measurements (*n* = 3 per group).

(H) Fluorescence intensity of Mito-Tracker Green detected using flow cytometry.

(I) Quantitative analysis of flow cytometric measurements (*n* = 3 per group). Two-tailed *p* values were calculated, and statistical significance was defined as $p < 0.05$, denoted as 'ns' for no statistical difference, and indicated as *$p < 0.05$, **$p < 0.01$, ***$p < 0.001$. All experiments and images shown are representative.

led to an elevated chondrocyte death rate, while crucial regulators of ferroptosis (such as ACSL4, TfR1, SLC7A11, and GPx4) showed marked alterations, ultimately resulting in ferroptosis. Following RSG intervention, intracellular iron/ROS/lipid ROS levels decreased, apoptosis was reduced, and there was downregulation of ACSL4/TfR1/CHAC1/4-HNE expression and upregulation of GPx4/SLC7A11/RGS4 expression. Furthermore, RSG increased GLUT1 expression, alleviating the disruption in glucose metabolism and energy supply caused by IL-1β. For the *in vivo* study, the IOOA model was established by intraperitoneal injection of ID combined with DMM surgery. The IOOA group exhibited accelerated cartilage degeneration, increased osteophytic formation, and higher expression of 4-HNE, ACSL4, COX-2, ADAMTS5, and MMP3 compared to the Sham and DMM groups. Following RSG intervention, cartilage deterioration was attenuated, osteophytic formation was limited, and the aforementioned elevated expression indicators were reduced, accompanied by upregulation of GPx4 and Nrf2. These results demonstrate that RSG serves as an effective ferroptosis suppressor in chondrocytes mediated by ACSL4, thereby protecting osteo-arthritic cartilage from destruction (Figure 10).

ACSL4, a distinctive and significant isozyme, plays a crucial role in regulating lipid biosynthesis by activating PUFAs.[73] PUFAs, serving as the primary substrates for lipid peroxidation in ferroptosis, are susceptible to oxidation, leading to the formation of PUFA hydroperox-ides.[74] ACSL4 enhances the susceptibility of PUFAs to oxidation, thus playing a critical role in the execution of ferroptosis. Additionally, ACSL4 contributes to the generation of phosphatidylethanolamine in the membrane through the esterification process of PUFAs to PUFA-CoA, significantly impacting lipid metabolism reprogramming in ferroptosis.[28] As a pivotal regulator, ACSL4 mediates ferroptosis by orchestrating lipid metabolism reprogramming and actively participates in the pathological processes of various diseases.[58] Recent studies have implicated ACSL4-mediated ferroptosis in OA.[75–81] Xu et al. illustrated that the upregulation of ACSL4 expression in the affected cartilage region exceeded that in the unaffected area, intensifying as human OA progressed.[80] In various preclinical OA models, ACSL4 protein levels were increased in IL-1β-stimulated chondrocytes.[75–79,81] Knockdown of ACSL4 mitigated the ferroptotic effects induced by IL-1β on chondrocytes.[75] These findings suggest that targeting ACSL4 could be a promising therapeutic approach for inter-vening in OA.

Herein, for the first time, we investigated the repurposing of RSG in an IOOA model. Compared to novel drugs, RSG may have a relatively short transition period from laboratory research to clinical application in the treatment of IOOA. As mentioned earlier, unlike other extensively studied forms of cell death, there is currently no standardized approach or biomarker for detecting ferroptosis.[19,52,82,83] To enhance meth-odological rigor, we employed a combination of multiple detection methods and various evaluation indicators for ferroptosis based on the experience of predecessors.

Conclusion

Within the present investigation, the introduction of RSG effectively alleviated inflammatory and iron overload-induced cartilage impairment, as evidenced in both *in vitro* and *in vivo* settings. Chondrocytes exposed to models of inflammation or iron overload exhibited disrupted iron metabolism and redox imbalance, resulting in lipid peroxidation and damage to membrane-containing organelles. This process compro-mised cell function and eventually led to ferroptosis. RSG exerted its chondroprotective and anti-ferroptotic effects by pharmacologically targeting ACSL4 activity, suppressing lipid peroxidation, and restoring iron homeostasis. While further investigation is needed to fully under-stand the underlying mechanisms, the results presented in this study introduce a promising new drug candidate for preventing and treat-ing IOOA.

Limitations of the study

However, certain limitations need acknowledgment. First, structural and regenerative differences between mouse chondrocytes and human chondrocytes suggest that the findings may not be directly applicable to humans. Second, although the clinical progression of IOOA typically extends over years or even decades, our *in vitro* intervention was confined to 48 h, and the *in vivo* experiment was conducted over a relatively short period of 10 weeks. Despite observing the *in vivo* biosafety of RSG local injection into the joint cavity, the safety of long-term RSG ap-plications still needs investigation in future studies. Finally, due to the estrus and menstrual cycles present in female mice, which may introduce problematic variables into scientific experiments and data analysis, this study exclusively employed male mice. Nevertheless, given the sta-tistically significant outcomes, we are optimistic about the potential of RSG in the treatment of IOOA and deem it worthy of additional scrutiny.
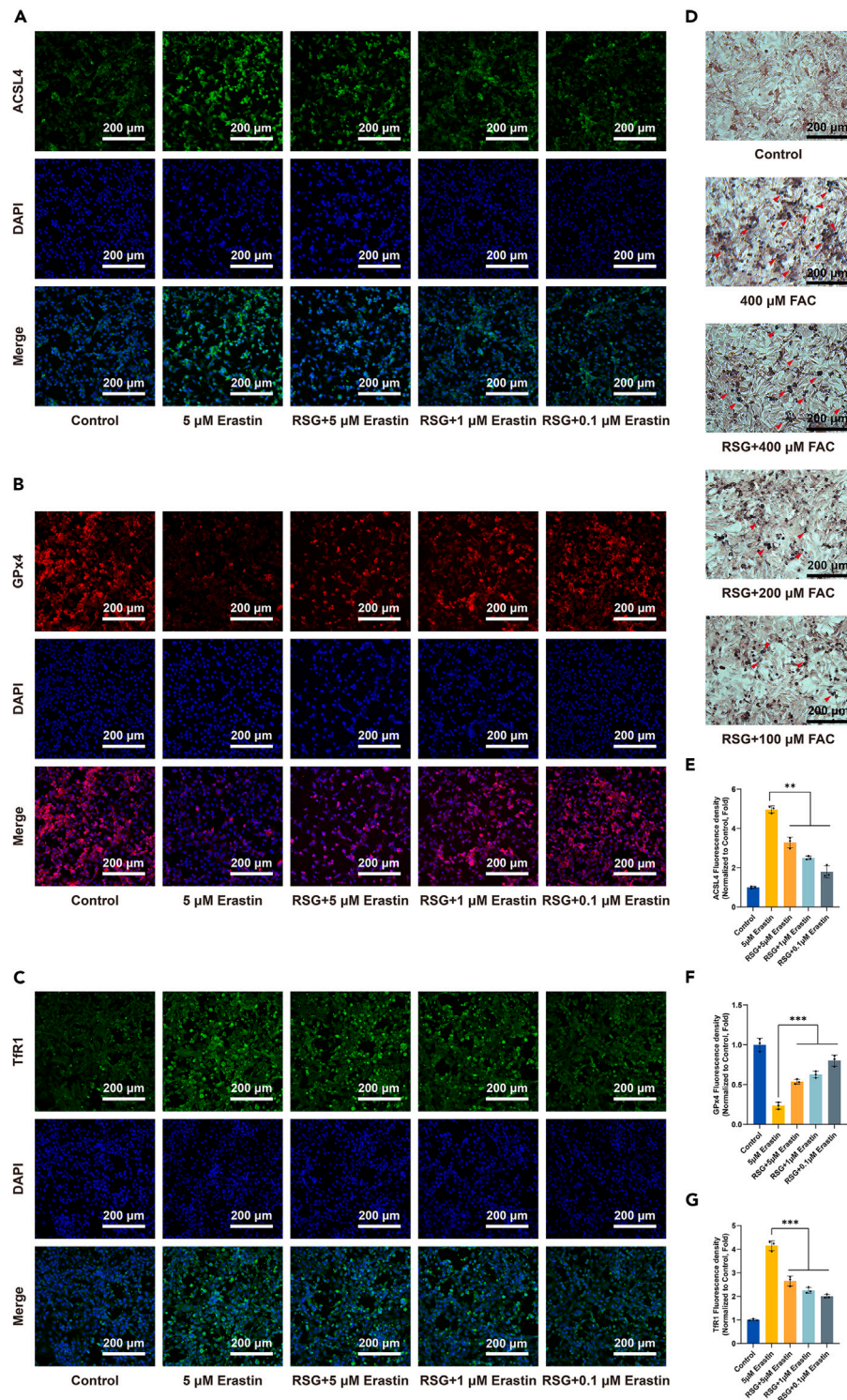
Figure 7. RSG preconditioning confers anti-ferroptotic property upon chondrocytes

(A–C) Immunofluorescence staining of ACSL4, GPx4, and TfR1 (scale bar = 200 μm).

(D) Prussian blue staining was performed on chondrocytes, with red arrows indicating iron deposition (scale bar = 200 μm).

(E–G) Quantification of immunofluorescence staining for ACSL4, GPx4, and TfR1 (n = 3 per group). Two-tailed p values were calculated, and statistical significance was defined as $p < 0.05$, denoted as 'ns' for no statistical difference, and indicated as *$p < 0.05$, **$p < 0.01$, ***$p < 0.001$. All experiments and images shown are representative.
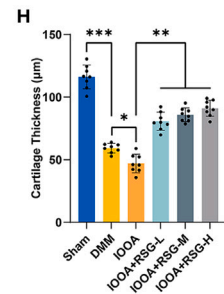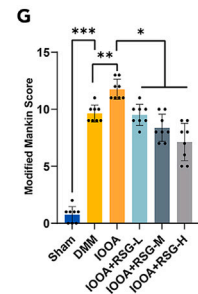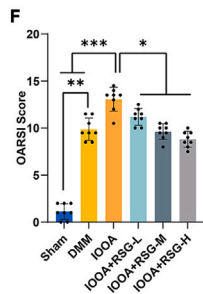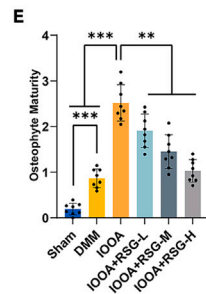
Figure 8. RSG attenuates cartilage degeneration *in vivo*

(A) Schematic diagram illustrating the experimental design with animals. This figure was created using Figdraw (https://www.figdraw.com/static/index.html#/).

(B) Three-dimensional sagittal and coronal images of mouse knee joints reconstructed using micro-CT, with the red arrow indicating osteophyte formation (scale bar = 1 mm).
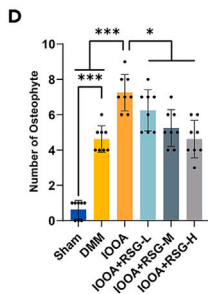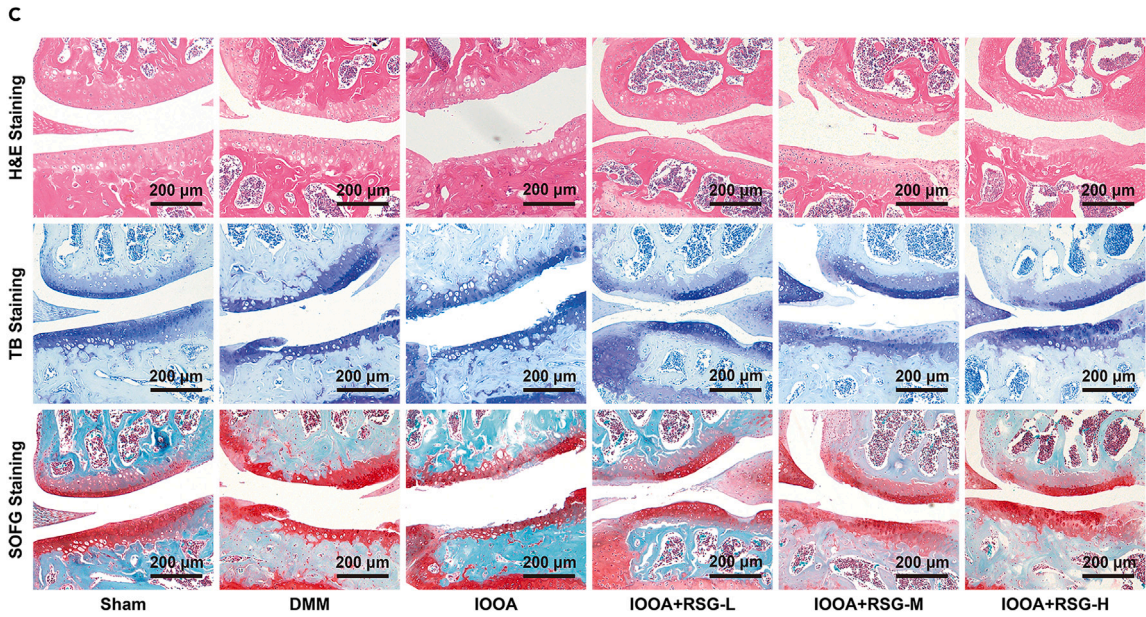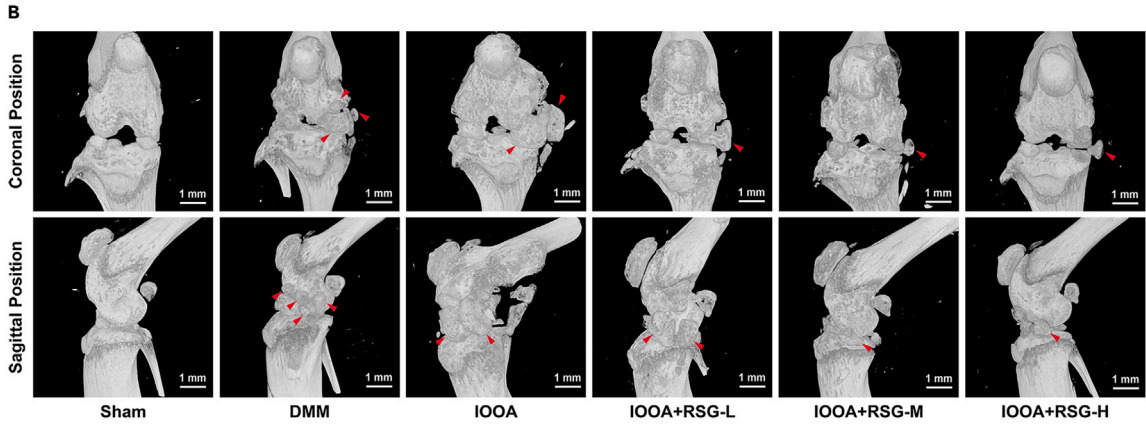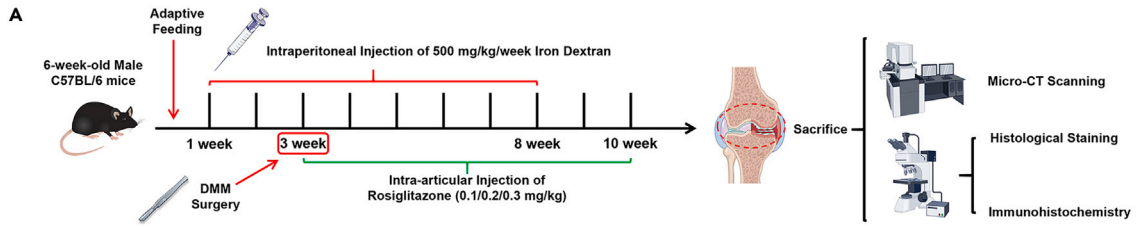
(C) Histological assessments, including H&E, TB, and SOFG staining, of knee sections from each group (scale bar = 200 μm).

(D) Quantification of articular osteophytes in each group ($n = 8$ per group).

(E) Quantitative analysis of osteophyte maturity in each group ($n = 8$ per group). (F) OARSI scores for the six groups of mice ($n = 8$ per group).

(G) Modified Mankin scores for each group ($n = 8$ per group).

(H) Measurement of cartilage thickness in knee joints among the six groups ($n = 8$ per group). Two-tailed p values were calculated, and statistical significance was defined as $p < 0.05$, denoted as 'ns' for no statistical difference, and indicated as $*p < 0.05$, $**p < 0.01$, $***p < 0.001$. All experiments and images shown are representative.

STAR★METHODS

Detailed methods are provided in the online version of this paper and include the following:

- KEY RESOURCES TABLE
- RESOURCE AVAILABILITY
  - Lead contact
  - Materials availability
  - Data and code availability
- EXPERIMENTAL MODEL AND STUDY PARTICIPANT DETAILS
  - Animal experiments
- METHOD DETAILS
  - Chondrocytes preparation and treatment
  - Cell counting Kit-8 (**CCK-8**) assay
  - Toluidine blue (TB) staining
  - 5-Ethynyl-20-Deoxyuridine (EdU) staining assay
  - Live/dead cell staining
  - Apoptosis detection
  - Senescence-associated β-galactosidase (SA-β-Gal) staining assay
  - Intracellular iron assay
  - Detection of reactive oxygen species (ROS) and lipid peroxidation
  - Measurement of reduced glutathione (GSH) and oxidized glutathione Disulfide (GSSG)
  - Glutamine and glutamate assays
  - Superoxide dismutase (SOD) activity
  - Mitochondrial membrane potential
  - Fluorescence staining of the membrane-containing organelles
  - Transmission electron microscope (TEM)
  - Quantitative Real-time PCR (qPCR)
  - Protein extraction and Western Blot
  - Enzyme-linked immunosorbent assay (ELISA)
  - Immunofluorescence (IF)
  - ACSL4 small interfering RNA (siRNA) transfection
  - Glucose content detection
  - Molecular docking
  - Micro-computed tomography (micro-CT)
  - Histological staining
  - Immunohistochemical (IHC) staining
  - *In vivo* biosafety assessment of RSG intra-articular injection
- QUANTIFICATION AND STATISTICAL ANALYSIS

SUPPLEMENTAL INFORMATION

Supplemental information can be found online at https://doi.org/10.1016/j.isci.2024.110526.

ACKNOWLEDGMENTS
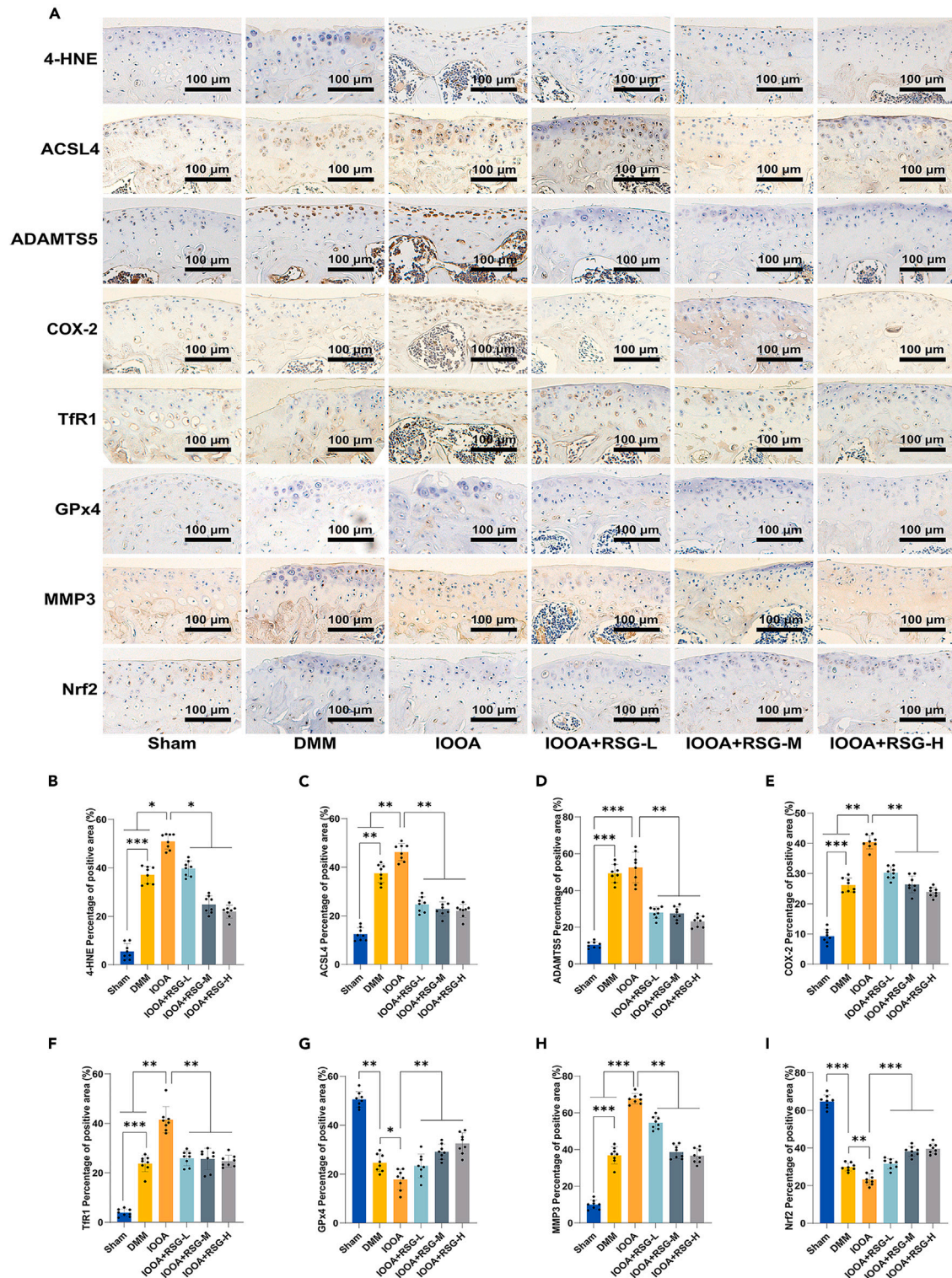
Figure 9. RSG alleviated chondrocyte inflammatory responses, ECM degradation, and ferroptosis within the surgery-induced mouse OA model

(A) IHC assay of 4-HNE, ACSL4, ADAMTS5, COX-2, TfR1, GPx4, MMP3, and Nrf2 in articular cartilage of each group (scale bar = 100 μm).

(B–I) Quantification of IHC analysis of 4-HNE, ACSL4, ADAMTS5, COX-2, TfR1, GPx4, MMP3, and Nrf2 (n = 8 per group). Two-tailed p values were calculated, and statistical significance was defined as $p < 0.05$, denoted as 'ns' for no statistical difference, and indicated as *$p < 0.05$, **$p < 0.01$, ***$p < 0.001$. All experiments and images shown are representative.
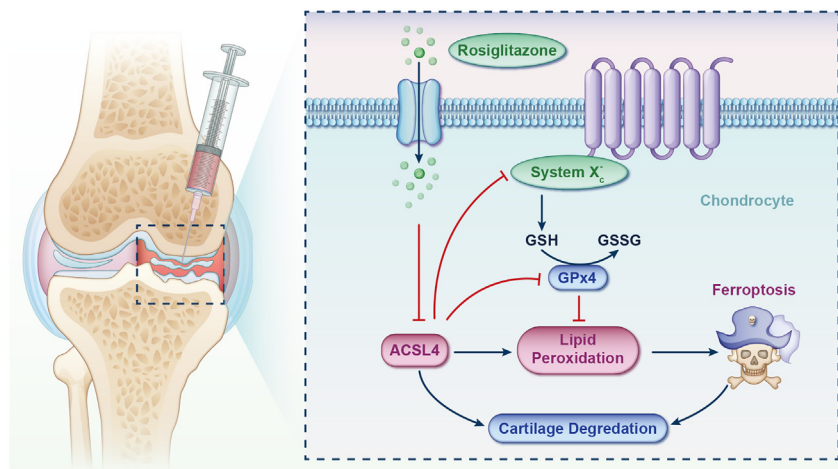
Figure 10. A graphical abstract illustrating the role of RSG in retarding the progression of iron overload-induced osteoarthritis by impeding chondrocyte ferroptosis

AUTHOR CONTRIBUTIONS

S.Y.C. and Y.H.W.: Conceptualization, Investigation, Methodology, and Writing – Original Draft. Y.H.Y. and Y.Q.C.: Data curation, Visualization, Writing – Review and Editing, and Formal analysis. J.Y.Q. and D.L.W.: Validation, Software, Supervision. A.X., P.L., and H.Z.: Project administration, Funding acquisition, and Resources.

DECLARATION OF INTERESTS

The authors declare no competing interests.

REFERENCES

1. Hunter, D.J., and Bierma-Zeinstra, S. (2019). Osteoarthritis. Lancet (London, England) *393*, 1745–1759. https://doi.org/10.1016/s0140-6736(19)30417-9.

2. Hunter, D.J., March, L., and Chew, M. (2020). Osteoarthritis in 2020 and beyond: a Lancet Commission. Lancet (London, England) *396*, 1711–1712. https://doi.org/10.1016/s0140-6736(20)32230-3.

3. O'Neill, T.W., McCabe, P.S., and McBeth, J. (2018). Update on the epidemiology, risk factors and disease outcomes of osteoarthritis. Best practice & research. Clin. Rheumatol. *32*, 312–326. https://doi.org/10.1016/j.berh.2018.10.007.

4. Chen, D., Shen, J., Zhao, W., Wang, T., Han, L., Hamilton, J.L., and Im, H.J. (2017). Osteoarthritis: toward a comprehensive understanding of pathological mechanism. Bone Res. *5*, 16044. https://doi.org/10.1038/boneres.2016.44.

5. GBD 2021 Osteoarthritis Collaborators (2023). Global, regional, and national burden of osteoarthritis, 1990-2020 and projections to 2050: a systematic analysis for the Global Burden of Disease Study 2021. Lancet. Rheumatol. *5*, e508–e522. https://doi.org/10.1016/s2665-9913(23)00163-7.

6. Yuan, C., Pan, Z., Zhao, K., Li, J., Sheng, Z., Yao, X., Liu, H., Zhang, X., Yang, Y., Yu, D., et al. (2020). Classification of four distinct osteoarthritis subtypes with a knee joint tissue transcriptome atlas. Bone Res. *8*, 38. https://doi.org/10.1038/s41413-020-00109-x.

7. Sherwood, J. (2019). Osteoarthritis year in review 2018: biology. Osteoarthritis Cartilage *27*, 365–370. https://doi.org/10.1016/j.joca.2018.10.005.

8. Sun, K., Guo, Z., Hou, L., Xu, J., Du, T., Xu, T., and Guo, F. (2021). Iron homeostasis in arthropathies: From pathogenesis to therapeutic potential. Ageing Res. Rev. *72*, 101481. https://doi.org/10.1016/j.arr.2021.101481.

9. Ru, Q., Li, Y., Xie, W., Ding, Y., Chen, L., Xu, G., Wu, Y., and Wang, F. (2023). Fighting age-related orthopedic diseases: focusing on ferroptosis. Bone Res. *11*, 12. https://doi.org/10.1038/s41413-023-00247-y.

10. Cai, C., Hu, W., and Chu, T. (2021). Interplay Between Iron Overload and Osteoarthritis: Clinical Significance and Cellular Mechanisms. Front. Cell Dev. Biol. *9*, 817104. https://doi.org/10.3389/fcell.2021.817104.

11. Kennish, L., Attur, M., Oh, C., Krasnokutsky, S., Samuels, J., Greenberg, J.D., Huang, X., and Abramson, S.B. (2014). Age-dependent ferritin elevations and HFE C282Y mutation as risk factors for symptomatic knee osteoarthritis in males: a longitudinal cohort study. BMC Musculoskelet. Disord. *15*, 8. https://doi.org/10.1186/1471-2474-15-8.

12. Xu, J., Zhang, S., Tian, Y., Si, H., Zeng, Y., Wu, Y., Liu, Y., Li, M., Sun, K., Wu, L., and Shen, B. (2022). Genetic Causal Association between Iron Status and Osteoarthritis: A Two-Sample Mendelian Randomization. Nutrients *14*, 3683. https://doi.org/10.3390/nu14183683.

13. Zhang, S., Xu, J., Si, H., Wu, Y., Zhou, S., and Shen, B. (2022). The Role Played by Ferroptosis in Osteoarthritis: Evidence Based on Iron Dyshomeostasis and Lipid Peroxidation. Antioxidants *11*, 1668. https://doi.org/10.3390/antiox11091668.

14. Chen, B., Wang, L., Xie, D., and Wang, Y. (2024). Exploration and breakthrough in the mode of chondrocyte death - A potential new mechanism for osteoarthritis. Biomed. Pharmacother. *170*, 115990. https://doi.org/10.1016/j.biopha.2023.115990.

15. Chen, H., Han, Z., Wang, Y., Su, J., Lin, Y., Cheng, X., Liu, W., He, J., Fan, Y., Chen, L., and Zuo, H. (2023). Targeting Ferroptosis in Bone-Related Diseases: Facts and Perspectives. J. Inflamm. Res. *16*, 4661–4677. https://doi.org/10.2147/jir.S432111.

16. Liang, D., Minikes, A.M., and Jiang, X. (2022). Ferroptosis at the intersection of lipid metabolism and cellular signaling. Mol. Cell *82*, 2215–2227. https://doi.org/10.1016/j.molcel.2022.03.022.

17. Ni, Z., Li, Y., Song, D., Ding, J., Mei, S., Sun, S., Cheng, W., Yu, J., Zhou, L., Kuang, Y., et al. (2022). Iron-overloaded follicular fluid increases the risk of endometriosis-related infertility by triggering granulosa cell ferroptosis and oocyte dysmaturity. Cell Death Dis. *13*, 579. https://doi.org/10.1038/s41419-022-05037-8.

18. Yang, J., Hu, S., Bian, Y., Yao, J., Wang, D., Liu, X., Guo, Z., Zhang, S., and Peng, L. (2021). Targeting Cell Death: Pyroptosis, Ferroptosis, Apoptosis and Necroptosis in Osteoarthritis. Front. Cell Dev. Biol. *9*, 789948. https://doi.org/10.3389/fcell.2021.789948.

19. Cao, S., Wei, Y., Xu, H., Weng, J., Qi, T., Yu, F., Liu, S., Xiong, A., Liu, P., and Zeng, H. (2023). Crosstalk between ferroptosis and chondrocytes in osteoarthritis: a systematic review of in vivo and in vitro studies. Front. Immunol. *14*, 1202436. https://doi.org/10.3389/fimmu.2023.1202436.

20. Pan, Z., He, Q., Zeng, J., Li, S., Li, M., Chen, B., Yang, J., Xiao, J., Zeng, C., Luo, H., and Wang, H. (2022). Naringenin protects against iron overload-induced osteoarthritis by suppressing oxidative stress. Phytomedicine *105*, 154330. https://doi.org/10.1016/j.phymed.2022.154330.

21. He, Q., Yang, J., Pan, Z., Zhang, G., Chen, B., Li, S., Xiao, J., Tan, F., Wang, Z., Chen, P., and Wang, H. (2023). Biochanin A protects against iron overload associated knee osteoarthritis via regulating iron levels and NRF2/System xc-/GPX4 axis. Biomed. Pharmacother. *157*, 113915. https://doi.org/10.1016/j.biopha.2022.113915.

22. Li, S., He, Q., Chen, B., Zeng, J., Dou, X., Pan, Z., Xiao, J., Li, M., Wang, F., Chen, C., et al. (2023). Cardamonin protects against iron overload induced arthritis by attenuating ROS production and NLRP3 inflammasome activation via the SIRT1/p38MAPK signaling pathway. Sci. Rep. *13*, 13744. https://doi.org/10.1038/s41598-023-40930-y.

23. Jing, X., Wang, Q., Du, T., Zhang, W., Liu, X., Liu, Q., Li, T., Wang, G., Chen, F., and Cui, X. (2021). Calcium chelator BAPTA-AM protects against iron overload-induced chondrocyte mitochondrial dysfunction and cartilage degeneration. Int. J. Mol. Med. *48*, 196. https://doi.org/10.3892/ijmm.2021.5029.

24. Kagan, V.E., Mao, G., Qu, F., Angeli, J.P.F., Doll, S., Croix, C.S., Dar, H.H., Liu, B., Tyurin, V.A., Ritov, V.B., et al. (2017). Oxidized arachidonic and adrenic PEs navigate cells to ferroptosis. Nat. Chem. Biol. *13*, 81–90. https://doi.org/10.1038/nchembio.2238.

25. Golej, D.L., Askari, B., Kramer, F., Barnhart, S., Vivekanandan-Giri, A., Pennathur, S., and Bornfeldt, K.E. (2011). Long-chain acyl-CoA synthetase 4 modulates prostaglandin E(2) release from human arterial smooth muscle cells. J. Lipid Res. *52*, 782–793. https://doi.org/10.1194/jlr.M013292.

26. Hadian, K., and Stockwell, B.R. (2023). The therapeutic potential of targeting regulated non-apoptotic cell death. Nat. Rev. Drug Discov. *22*, 723–742. https://doi.org/10.1038/s41573-023-00749-8.

27. Pope, L.E., and Dixon, S.J. (2023). Regulation of ferroptosis by lipid metabolism. Trends Cell Biol. *33*, 1077–1087. https://doi.org/10.1016/j.tcb.2023.05.003.

28. Doll, S., Proneth, B., Tyurina, Y.Y., Panzilius, E., Kobayashi, S., Ingold, I., Irmler, M., Beckers, J., Aichler, M., Walch, A., et al. (2017). ACSL4 dictates ferroptosis sensitivity by shaping cellular lipid composition. Nat. Chem. Biol. *13*, 91–98. https://doi.org/10.1038/nchembio.2239.

29. Askari, B., Kanter, J.E., Sherrid, A.M., Golej, D.L., Bender, A.T., Liu, J., Hsueh, W.A., Beavo, J.A., Coleman, R.A., and Bornfeldt, K.E. (2007). Rosiglitazone inhibits acyl-CoA synthetase activity and fatty acid partitioning to diacylglycerol and triacylglycerol via a peroxisome proliferator-activated receptor-gamma-independent mechanism in human arterial smooth muscle cells and macrophages. Diabetes, Metab. Syndrome Obes. Targets Ther. *56*, 1143–1152. https://doi.org/10.2337/db06-0267.

30. Xu, Y., Li, X., Cheng, Y., Yang, M., and Wang, R. (2020). Inhibition of ACSL4 attenuates ferroptotic damage after pulmonary ischemia-reperfusion. FASEB J. *34*, 16262–16275. https://doi.org/10.1096/fj.202001758R.

31. Sun, S., Shen, J., Jiang, J., Wang, F., and Min, J. (2023). Targeting ferroptosis opens new avenues for the development of novel therapeutics. Signal Transduct. Target. Ther. *8*, 372. https://doi.org/10.1038/s41392-023-01606-1.

32. Jing, X., Lin, J., Du, T., Jiang, Z., Li, T., Wang, G., Liu, X., Cui, X., and Sun, K. (2020). Iron Overload Is Associated With Accelerated Progression of Osteoarthritis: The Role of DMT1 Mediated Iron Homeostasis. Front. Cell Dev. Biol. *8*, 594509. https://doi.org/10.3389/fcell.2020.594509.

33. Yao, X., Sun, K., Yu, S., Luo, J., Guo, J., Lin, J., Wang, G., Guo, Z., Ye, Y., and Guo, F. (2021). Chondrocyte ferroptosis contribute to the progression of osteoarthritis. J. Orthop. Translat. *27*, 33–43. https://doi.org/10.1016/j.jot.2020.09.006.

34. Blom, A.B., van Lent, P.L., Libregts, S., Holthuysen, A.E., van der Kraan, P.M., van Rooijen, N., and van den Berg, W.B. (2007). Crucial role of macrophages in matrix metalloproteinase-mediated cartilage destruction during experimental osteoarthritis: involvement of matrix metalloproteinase 3. Arthritis Rheum. *56*, 147–157. https://doi.org/10.1002/art.22337.

35. Glasson, S.S., Askew, R., Sheppard, B., Carito, B., Blanchet, T., Ma, H.L., Flannery, C.R., Peluso, D., Kanki, K., Yang, Z., et al. (2005). Deletion of active ADAMTS5 prevents cartilage degradation in a murine model of osteoarthritis. Nature *434*, 644–648. https://doi.org/10.1038/nature03369.

36. Stockwell, B.R. (2022). Ferroptosis turns 10: Emerging mechanisms, physiological functions, and therapeutic applications. Cell *185*, 2401–2421. https://doi.org/10.1016/j.cell.2022.06.003.

37. Miao, Y., Chen, Y., Xue, F., Liu, K., Zhu, B., Gao, J., Yin, J., Zhang, C., and Li, G. (2022). Contribution of ferroptosis and GPX4's dual functions to osteoarthritis progression. EBioMedicine *76*, 103847. https://doi.org/10.1016/j.ebiom.2022.103847.

38. Wang, X., Zhou, Y., Min, J., and Wang, F. (2023). Zooming in and out of ferroptosis in human disease. Front. Med. *17*, 173–206. https://doi.org/10.1007/s11684-023-0992-z.

39. Sun, K., Hou, L., Guo, Z., Wang, G., Guo, J., Xu, J., Zhang, X., and Guo, F. (2023). JNK-JUN-NCOA4 axis contributes to chondrocyte ferroptosis and aggravates osteoarthritis via ferritinophagy. Free Radic. Biol. Med. *200*, 87–101. https://doi.org/10.1016/j.freeradbiomed.2023.03.008.

40. Sun, K., Luo, J., Jing, X., Xiang, W., Guo, J., Yao, X., Liang, S., Guo, F., and Xu, T. (2021). Hyperoside ameliorates the progression of osteoarthritis: An in vitro and in vivo study. Phytomedicine *80*, 153387. https://doi.org/10.1016/j.phymed.2020.153387.

41. Jin, L., Alesi, G.N., and Kang, S. (2016). Glutaminolysis as a target for cancer therapy. Oncogene *35*, 3619–3625. https://doi.org/10.1038/onc.2015.447.

42. Zhang, X., Hou, L., Guo, Z., Wang, G., Xu, J., Zheng, Z., Sun, K., and Guo, F. (2023). Lipid peroxidation in osteoarthritis: focusing on 4-hydroxynonenal, malondialdehyde, and ferroptosis. Cell Death Discov. *9*, 320. https://doi.org/10.1038/s41420-023-01613-9.

43. Dixon, S.J., Lemberg, K.M., Lamprecht, M.R., Skouta, R., Zaitsev, E.M., Gleason, C.E., Patel, D.N., Bauer, A.J., Cantley, A.M., Yang, W.S., et al. (2012). Ferroptosis: an iron-dependent form of nonapoptotic cell death. Cell *149*, 1060–1072. https://doi.org/10.1016/j.cell.2012.03.042.

44. Gao, M., Yi, J., Zhu, J., Minikes, A.M., Monian, P., Thompson, C.B., and Jiang, X. (2019). Role of Mitochondria in Ferroptosis. Mol. Cell *73*, 354–363.e3. https://doi.org/10.1016/j.molcel.2018.10.042.

45. Fang, X., Wang, H., Han, D., Xie, E., Yang, X., Wei, J., Gu, S., Gao, F., Zhu, N., Yin, X., et al. (2019). Ferroptosis as a target for protection against cardiomyopathy. Proc. Natl. Acad.

Sci. USA *116*, 2672–2680. https://doi.org/10.1073/pnas.1821022116.

46. Gaschler, M.M., Andia, A.A., Liu, H., Csuka, J.M., Hurlocker, B., Vaiana, C.A., Heindel, D.W., Zuckerman, D.S., Bos, P.H., Reznik, E., et al. (2018). FINO(2) initiates ferroptosis through GPX4 inactivation and iron oxidation. Nat. Chem. Biol. *14*, 507–515. https://doi.org/10.1038/s41589-018-0031-6.

47. Wu, Y., Zhang, S., Gong, X., Tam, S., Xiao, D., Liu, S., and Tao, Y. (2020). The epigenetic regulators and metabolic changes in ferroptosis-associated cancer progression. Mol. Cancer *19*, 39. https://doi.org/10.1186/s12943-020-01157-x.

48. Pi, P., Zeng, L., Zeng, Z., Zong, K., Han, B., Bai, X., and Wang, Y. (2024). The role of targeting glucose metabolism in chondrocytes in the pathogenesis and therapeutic mechanisms of osteoarthritis: a narrative review. Front. Endocrinol. *15*, 1319827. https://doi.org/10.3389/fendo.2024.1319827.

49. Phillips, T., Ferraz, I., Bell, S., Clegg, P.D., Carter, S.D., and Mobasheri, A. (2005). Differential regulation of the GLUT1 and GLUT3 glucose transporters by growth factors and pro-inflammatory cytokines in equine articular chondrocytes. Vet. J. *169*, 216–222. https://doi.org/10.1016/j.tvjl.2004.01.026.

50. Shikhman, A.R., Brinson, D.C., Valbracht, J., and Lotz, M.K. (2001). Cytokine regulation of facilitated glucose transport in human articular chondrocytes. J. Immunol. *167*, 7001–7008. https://doi.org/10.4049/jimmunol.167.12.7001.

51. Shikhman, A.R., Brinson, D.C., and Lotz, M.K. (2004). Distinct pathways regulate facilitated glucose transport in human articular chondrocytes during anabolic and catabolic responses. Am. J. Physiol. Endocrinol. Metab. *286*, E980–E985. https://doi.org/10.1152/ajpendo.00243.2003.

52. Cao, S., Wei, Y., Yue, Y., Liu, P., and Zeng, H. (2023). Global research landscape on the crosstalk between ferroptosis and musculoskeletal diseases: A bibliometric and visualized analysis. Heliyon 9, e23113. https://doi.org/10.1016/j.heliyon.2023.e23113.

53. Doll, S., and Conrad, M. (2017). Iron and ferroptosis: A still ill-defined liaison. IUBMB Life *69*, 423–434. https://doi.org/10.1002/iub.1616.

54. Ding, K., Liu, C., Li, L., Yang, M., Jiang, N., Luo, S., and Sun, L. (2023). Acyl-CoA synthase ACSL4: an essential target in ferroptosis and fatty acid metabolism. Chin. Med. J. *136*, 2521–2537. https://doi.org/10.1097/cm9.0000000000002533.

55. Jia, B., Li, J., Song, Y., and Luo, C. (2023). ACSL4-Mediated Ferroptosis and Its Potential Role in Central Nervous System Diseases and Injuries. Int. J. Mol. Sci. *24*, 10021. https://doi.org/10.3390/ijms241210021.

56. Yang, Y., Zhu, T., Wang, X., Xiong, F., Hu, Z., Qiao, X., Yuan, X., and Wang, D. (2022). ACSL3 and ACSL4, Distinct Roles in Ferroptosis and Cancers. Cancers *14*, 5896. https://doi.org/10.3390/cancers14235896.

57. Kim, J.H., Lewin, T.M., and Coleman, R.A. (2001). Expression and characterization of recombinant rat Acyl-CoA synthetases 1, 4, and 5. Selective inhibition by triacsin C and thiazolidinediones. J. Biol. Chem. *276*, 24667–24673. https://doi.org/10.1074/jbc.M010793200.

58. Dai, Y., Chen, Y., Mo, D., Jin, R., Huang, Y., Zhang, L., Zhang, C., Gao, H., and Yan, Q. (2023). Inhibition of ACSL4 ameliorates tubular ferroptotic cell death and protects against fibrotic kidney disease. Commun. Biol. *6*, 907. https://doi.org/10.1038/s42003-023-05272-5.

59. Yang, J., Shi, X., Wang, Y., Ma, M., Liu, H., Wang, J., and Xu, Z. (2023). Multi-Target Neuroprotection of Thiazolidinediones on Alzheimer's Disease via Neuroinflammation and Ferroptosis. J. Alzheimers Dis. *96*, 927–945. https://doi.org/10.3233/jad-230593.

60. Wang, Y., Zhang, M., Bi, R., Su, Y., Quan, F., Lin, Y., Yue, C., Cui, X., Zhao, Q., Liu, S., et al. (2022). ACSL4 deficiency confers protection against ferroptosis-mediated acute kidney injury. Redox Biol. *51*, 102262. https://doi.org/10.1016/j.redox.2022.102262.

61. Li, Y., Feng, D., Wang, Z., Zhao, Y., Sun, R., Tian, D., Liu, D., Zhang, F., Ning, S., Yao, J., and Tian, X. (2019). Ischemia-induced ACSL4 activation contributes to ferroptosis-mediated tissue injury in intestinal ischemia/reperfusion. Cell Death Differ. *26*, 2284–2299. https://doi.org/10.1038/s41418-019-0299-4.

62. Tao, W.H., Shan, X.S., Zhang, J.X., Liu, H.Y., Wang, B.Y., Wei, X., Zhang, M., Peng, K., Ding, J., Xu, S.X., et al. (2022). exmedetomidine Attenuates Ferroptosis-Mediated Renal Ischemia/Reperfusion Injury and Inflammation by Inhibiting ACSL4 via α2-AR. Front. Pharmacol. *13*, 782466. https://doi.org/10.3389/fphar.2022.782466.

63. Gao, L., Zhang, J., Yang, T., Jiang, L., Liu, X., Wang, S., Wang, X., Huang, Y., Wang, H., Zhang, M., et al. (2023). STING/ACSL4 axis-dependent ferroptosis and inflammation promote hypertension-associated chronic kidney disease. Mol. Ther. *31*, 3084–3103. https://doi.org/10.1016/j.ymthe.2023.07.026.

64. Xu, Y., Li, X., Cheng, Y., Yang, M., and Wang, R. (2020). Inhibition of ACSL4 attenuates ferroptotic damage after pulmonary ischemia-reperfusion. FASEB J. *34*, 16262–16275. https://doi.org/10.1096/fj.202001758R.

65. Wang, Y., Bi, R., Quan, F., Cao, Q., Lin, Y., Yue, C., Cui, X., Yang, H., Gao, X., and Zhang, D. (2020). Ferroptosis involves in renal tubular cell death in diabetic nephropathy. Eur. J. Pharmacol. *888*, 173574. https://doi.org/10.1016/j.ejphar.2020.173574.

66. Chen, J., Yang, L., Geng, L., He, J., Chen, L., Sun, Q., Zhao, J., and Wang, X. (2021). Inhibition of Acyl-CoA Synthetase Long-Chain Family Member 4 Facilitates Neurological Recovery After Stroke by Regulation Ferroptosis. Front. Cell. Neurosci. *15*, 632354. https://doi.org/10.3389/fncel.2021.632354.

67. Wei, S., Qiu, T., Wang, N., Yao, X., Jiang, L., Jia, X., Tao, Y., Zhang, J., Zhu, Y., Yang, G., et al. (2020). Ferroptosis mediated by the interaction between Mfn2 and IREα promotes arsenic-induced nonalcoholic steatohepatitis. Environ. Res. *188*, 109824. https://doi.org/10.1016/j.envres.2020.109824.

68. Liu, S., Tang, Y., Liu, L., Yang, L., Li, P., Liu, X., and Yin, H. (2022). Proteomic analysis reveals that ACSL4 activation during reflux esophagitis contributes to ferroptosis-mediated esophageal mucosal damage. Eur. J. Pharmacol. *931*, 175175. https://doi.org/10.1016/j.ejphar.2022.175175.

69. Wang, S., Li, X., Li, J., Wang, A., Li, F., Hu, H., Long, T., Pei, X., Li, H., Zhong, F., and Zhu, F. (2024). Inhibition of cisplatin-induced Acsl4-mediated ferroptosis alleviated ovarian injury. Chem. Biol. Interact. *387*, 110825. https://doi.org/10.1016/j.cbi.2023.110825.

70. Shen, J., Qian, M., Wu, M., Tang, J., Gong, Y., Li, J., Ji, J., and Dang, B. (2023). Rosiglitazone inhibits acyl-CoA synthetase long-chain family number 4 and improves secondary brain injury in a rat model of surgical brain injury. Clin. Exp. Pharmacol. Physiol. *50*, 927–935. https://doi.org/10.1111/1440-1681.13815.

71. Li, C., Wu, Y., Chen, K., Chen, R., Xu, S., Yang, B., Lian, Z., Wang, X., Wang, K., Xie, H., et al. (2023). Gp78 deficiency in hepatocytes alleviates hepatic ischemia-reperfusion injury via suppressing ACSL4-mediated ferroptosis. Cell Death Dis. *14*, 810. https://doi.org/10.1038/s41419-023-06294-x.

72. Jing, X., Du, T., Li, T., Yang, X., Wang, G., Liu, X., Jiang, Z., and Cui, X. (2021). The detrimental effect of iron on OA chondrocytes: Importance of pro-inflammatory cytokines induced iron influx and oxidative stress. J. Cell Mol. Med. *25*, 5671–5680. https://doi.org/10.1111/jcmm.16581.

73. Belavgeni, A., Meyer, C., Stumpf, J., Hugo, C., and Linkermann, A. (2020). Ferroptosis and Necroptosis in the Kidney. Cell Chem. Biol. *27*, 448–462. https://doi.org/10.1016/j.chembiol.2020.03.016.

74. Yang, W.S., Kim, K.J., Gaschler, M.M., Patel, M., Shchepinov, M.S., and Stockwell, B.R. (2016). Peroxidation of polyunsaturated fatty acids by lipoxygenases drives ferroptosis. Proc. Natl. Acad. Sci. USA *113*, E4966–E4975. https://doi.org/10.1073/pnas.1603244113.

75. He, W., Lin, X., and Chen, K. (2023). Specificity protein 1-mediated ACSL4 transcription promoted the osteoarthritis progression through suppressing the ferroptosis of chondrocytes. J. Orthop. Surg. Res. *18*, 188. https://doi.org/10.1186/s13018-023-03673-0.

76. Xu, W., Zhang, B., Xi, C., Qin, Y., Lin, X., Wang, B., Kong, P., and Yan, J. (2023). Ferroptosis Plays a Role in Human Chondrocyte of Osteoarthritis Induced by IL-1β. Cartilage *14*, 455–466. https://doi.org/10.1177/19476035221142011.

77. Kong, R., Ji, L., Pang, Y., Zhao, D., and Gao, J. (2023). Exosomes from osteoarthritic fibroblast-like synoviocytes promote cartilage ferroptosis and damage via delivering microRNA-19b-3p to target SLC7A11 in osteoarthritis. Front. Immunol. *14*, 1181156. https://doi.org/10.3389/fimmu.2023.1181156.

78. Zhou, Y., Jia, Z., Wang, J., Huang, S., Yang, S., Xiao, S., Xia, D., and Zhou, Y. (2023). Curcumin reverses erastin-induced chondrocyte ferroptosis by upregulating Nrf2. Heliyon 9, e20163. https://doi.org/10.1016/j.heliyon.2023.e20163.

79. Cheng, B., Zhang, J., Shen, Q., Sun, Z., Luo, Y., and Hu, Y. (2024). Liproxstatin-1 alleviates cartilage degradation by inhibiting chondrocyte ferroptosis in the temporomandibular joint. Biol. Cell *116*, e202300042. https://doi.org/10.1111/boc.202300042.

80. Xu, Y., Yang, Z., Dai, T., Xue, X., Xia, D., Feng, Z., Huang, J., Chen, X., Sun, S., Zhou, J., et al. (2023). Characteristics and time points to

inhibit ferroptosis in human osteoarthritis. Sci. Rep. *13*, 21592. https://doi.org/10.1038/s41598-023-49089-y.

81. Liu, J., Zhou, H., Chen, J., Zuo, Q., and Liu, F. (2024). Baicalin inhibits IL-1β-induced ferroptosis in human osteoarthritis chondrocytes by activating Nrf-2 signaling pathway. J. Orthop. Surg. Res. *19*, 23. https://doi.org/10.1186/s13018-023-04483-0.

82. Magtanong, L., and Dixon, S.J. (2018). Ferroptosis and Brain Injury. Dev. Neurosci. *40*, 382–395. https://doi.org/10.1159/000496922.

83. Cao, S., Wei, Y., Yue, Y., Chen, Y., Liao, S., Li, A., Liu, P., Xiong, A., and Zeng, H. (2024). Targeting ferroptosis unveils a new era for traditional Chinese medicine: a scientific metrology study. Front. Pharmacol. *15*, 1366852. https://doi.org/10.3389/fphar.2024.1366852.

84. Chen, P., Liu, X., Gu, C., Zhong, P., Song, N., Li, M., Dai, Z., Fang, X., Liu, Z., Zhang, J., et al. (2022). A plant-derived natural photosynthetic system for improving cell anabolism. Nature *612*, 546–554. https://doi.org/10.1038/s41586-022-05499-y.

85. Burton, L.H., Radakovich, L.B., Marolf, A.J., and Santangelo, K.S. (2020). Systemic iron overload exacerbates osteoarthritis in the strain 13 guinea pig. Osteoarthritis Cartilage *28*, 1265–1275. https://doi.org/10.1016/j.joca.2020.06.005.

86. Tsay, J., Yang, Z., Ross, F.P., Cunningham-Rundles, S., Lin, H., Coleman, R., Mayer-Kuckuk, P., Doty, S.B., Grady, R.W., Giardina, P.J., et al. (2010). Bone loss caused by iron overload in a murine model: importance of oxidative stress. Blood *116*, 2582–2589. https://doi.org/10.1182/blood-2009-12-260083.

87. O'Boyle, N.M., Banck, M., James, C.A., Morley, C., Vandermeersch, T., and Hutchison, G.R. (2011). Open Babel: An open chemical toolbox. J. Cheminform. *3*, 33. https://doi.org/10.1186/1758-2946-3-33.

88. Eberhardt, J., Santos-Martins, D., Tillack, A.F., and Forli, S. (2021). AutoDock Vina 1.2.0: New Docking Methods, Expanded Force Field, and Python Bindings. J. Chem. Inf. Model. *61*, 3891–3898. https://doi.org/10.1021/acs.jcim.1c00203.

89. Trott, O., and Olson, A.J. (2010). AutoDock Vina: improving the speed and accuracy of docking with a new scoring function, efficient optimization, and multithreading. J. Comput. Chem. *31*, 455–461. https://doi.org/10.1002/jcc.21334.

90. Rutgers, M., van Pelt, M.J.P., Dhert, W.J.A., Creemers, L.B., and Saris, D.B.F. (2010). Evaluation of histological scoring systems for tissue-engineered, repaired and osteoarthritic cartilage. Osteoarthritis Cartilage *18*, 12–23. https://doi.org/10.1016/j.joca.2009.08.009.

91. Glasson, S.S., Chambers, M.G., Van Den Berg, W.B., and Little, C.B. (2010). The OARSI histopathology initiative - recommendations for histological assessments of osteoarthritis in the mouse. Osteoarthritis Cartilage *18*, S17–S23. https://doi.org/10.1016/j.joca.2010.05.025.

STAR★METHODS

KEY RESOURCES TABLE

REAGENT or RESOURCE	SOURCE	IDENTIFIER
Antibodies		
MMP3	FineTest, Wuhan, China	FNab05244
ADAMTS5	Bioss, Beijing, China	bs-3573R
GLUT1	ABclonal, Wuhan, China	A6982
MMP13	FineTest, Wuhan, China	FNab05235
CHAC1	ABclonal, Wuhan, China	A15584
TfR1	FineTest, Wuhan, China	FNab08931
ACSL4	ABclonal, Wuhan, China	A20414
RGS4	FineTest, Wuhan, China	FNab07271
SLC7A11	FineTest, Wuhan, China	FNab10533
LPCAT3	ABclonal, Wuhan, China	A17604
GPx4	FineTest, Wuhan, China	FNab03622
COX-2	FineTest, Wuhan, China	FNab10407
4-HNE	Bioss, Beijing, China	bs-6313R
Nrf2	Servicebio, Wuhan, China	GB113808-100
Vinculin	FineTest, Wuhan, China	FNab09799
GAPDH	Cell Signaling Technology, Massachusetts, USA	5174S
FITC-conjugated Goat anti-Rabbit IgG (H + L)	ABclonal, Wuhan, China	AS011
Anti-rabbit IgG (H + L), F(ab')2 Fragment (Alexa Fluor® 555 Conjugate)	Cell Signaling Technology, Massachusetts, USA	4413S
HRP Goat Anti-Rabbit IgG (H + L)	ABclonal, Wuhan, China	AS014
Chemicals, peptides, and recombinant proteins		
Complete DMEM/F12 Medium	Procell, Wuhan, China	PM150310B
0.25% trypsin-EDTA	Servicebio, Wuhan, China	G4001
GP-transfect-Mate	GenePharma, Shanghai, China	G04009
Tissue Lysis Buffer for Glucose Assay	Beyotime, Shanghai, China	S3062
Cell Lysis Buffer	Beyotime, Shanghai, China	P0013
RIPA Lysis Buffer	Servicebio, Wuhan, China	G2033
PMSF	Servicebio, Wuhan, China	G2008
TBST Buffer	Servicebio, Wuhan, China	G2150
Super-sensitive ECL Chemiluminescent Substrate	Biosharp, Hefei, China	BL520B
Western Blot Running Buffer	Servicebio, Wuhan, China	G2144
Western Blot Transfer Buffer	Servicebio, Wuhan, China	G2145
10% SDS-PAGE	Biotides, Bejing, China	WB1102
4% Paraformaldehyde Fixative Tissue Fixation Fluid	Servicebio, Wuhan, China	G1101
4% Paraformaldehyde	Beyotime, Shanghai, China	P0099
Toluidine Blue Stain Solution for Cell	Solarbio, Beijing, China	G3660
Rosiglitazone	Rhawn, Shanghai, China	R014317
Erastin	Macklin, Shanghai, China	E872563
PBS buffer	Procell, Wuhan, China	PB180327
Ferric Ammonium Citrate	Rhawn, Shanghai, China	R017760

Continued

REAGENT or RESOURCE	SOURCE	IDENTIFIER
Recombinant Mouse Interleukin-1 beta	PeproTech, New Jersey, USA	211-11B
Iron Dextran	Macklin, Shanghai, China	I812123
TB Green® Premix DimerEraser™	Takara, Kyoto, Japan	RR091A
FerroOrange	Dojindo, Kumamoto, Japan	F374
Mito-FerroGreen	Dojindo, Kumamoto, Japan	M489
Lipid Peroxidation Probe-BDP 581/591 C11	Dojindo, Kumamoto, Japan	L267
Liperfluo	Dojindo, Kumamoto, Japan	L248
mtSOX Deep Red	Dojindo, Kumamoto, Japan	MT14
Mito-Tracker Green	Beyotime, Shanghai, China	C1048
LysoTracker red	Beyotime, Shanghai, China	C1046
ER-Tracker Green	Beyotime, Shanghai, China	C1042S
Golgi-Tracker Red	Beyotime, Shanghai, China	C1043
Toluidine Blue Cartilage Stain Solution	Servicebio, Wuhan, China	G1032
Saffron-O and Fast Green Stain Solution	Servicebio, Wuhan, China	G1053
Hematoxylin-Eosin Stain Solution	Servicebio, Wuhan, China	G1005
Isoflurane	RWD Life Science	R510-22
DAB Stain Solution	Servicebio, Wuhan, China	G1212
Dimethyl sulfoxide	Solarbio, Beijing, China	D8371
Critical commercial assays		
Glucose assay kit with O-toluidine	Beyotime, Shanghai, China	S0201S
Bicinchoninic Acid Protein Assay Kit	KeyGEN BioTECH, Nanjing, China	KGB2101
Cell Counting Kit-8	Beyotime, Shanghai, China	C0037
Total RNA Isolation Kit	Beibei Biotechnology, Zhengzhou, China	082001
PrimeScript™ RT Reagent Kit with gDNA Eraser	Takara, Kyoto, Japan	RR047A
Annexin V-FITC/Propidium Iodide Apoptosis Detection Kit	Dojindo, Kumamoto, Japan	AD10
Calcein-AM/PI Double Staining Kit	Dojindo, Kumamoto, Japan	C542
BeyoClick™ EdU Cell Proliferation Kit with Alexa Fluor 555	Beyotime, Shanghai, China	C0075S
Senescence-Associated β-Galactosidase Staining Kit	Solarbio, Beijing, China	G1580
Prussian Blue Iron Stain Kit for Cell	Solarbio, Beijing, China	G1426
Reactive Oxygen Species Assay Kit	Beyotime, Shanghai, China	S0033S
GSH and GSSG Assay Kit	Beyotime, Shanghai, China	S0053
Malondialdehyde Assay Kit	Beyotime, Shanghai, China	S0131S
Ferrous Ion Content Assay Kit	Solarbio, Beijing, China	BC5410
Glutamate Content Assay Kit	Solarbio, Beijing, China	BC1585
Glutamine Content Assay Kit	Geruisi, Soochow, China	G0429W
Superoxide Dismutase Activity Assay Kit	Solarbio, Beijing, China	BC5165
Mitochondrial Membrane Potential Assay Kit with JC-1	Beyotime, Shanghai, China	C2006
Mitochondrial Membrane Potential Assay Kit with Rhodamine 123	Beyotime, Shanghai, China	C2008S
Ultra-Sensitive TM SP (Mouse/Rabbit) IHC Kit	MXB Biotechnologies, Fuzhou, China	KIT-9710
Pepsin Antigen Repair Solution	Servicebio, Wuhan, China	G0142
Mouse 4-Hydroxynonenal ELISA Kit	FineTest, Wuhan, China	EM1583
Mouse Nitric Oxide Synthase 2 (iNOS) ELISA Kit	FineTest, Wuhan, China	EM0272
Mouse Phospholipid Hydroperoxide Glutathione peroxidase (GPx4) ELISA Kit	FineTest, Wuhan, China	EM1964

Continued

REAGENT or RESOURCE	SOURCE	IDENTIFIER
Mouse Interleukin-6 (IL-6) ELISA Kit	ABclonal, Wuhan, China	RK00008
Mouse Cyclooxygenase-2 (COX-2) ELISA Kit	ABclonal, Wuhan, China	RK03142
Mouse Tumor Necrosis Factor-alpha (TNF-α) ELISA Kit	ABclonal, Wuhan, China	RK00027
Experimental models: Cell lines		
Primary mouse chondrocytes	Procell, Wuhan, China	CP-M087
Experimental models: Organisms/strains		
C57BL/6 mice	Guangdong Medical Laboratory Animal Center	Not Applicable
Oligonucleotides		
Primer for qPCR	Table S1	Not Applicable
Software and algorithms		
ImageJ/Fiji 2.9.0	National Institutes of Health	https://imagej.net/ij/
GraphPad Prism 9.5	GraphPad Software, San Diego, USA	https://www.graphpad.com/
G*Power 3.1.9.7	Universität Düsseldorf, Germany	https://www.psychologie.hhu.de/arbeitsgruppen/allgemeine-psychologie-und-arbeitspsychologie/gpower

RESOURCE AVAILABILITY

Lead contact

Further information and reasonable requests for reagents and resources should be directed to and will be fulfilled by the lead contact, Hui Zeng (zenghui@pkuszh.com).

Materials availability

The study did not generate new unique reagents.

Data and code availability

- All data reported in this paper will be available from the lead contact upon reasonable request.
- This paper does not include original code.
- Any additional information needed to reanalyze the data is available from the lead contact upon reasonable request.

EXPERIMENTAL MODEL AND STUDY PARTICIPANT DETAILS

Animal experiments

When determining the minimum number of animals required for the present study, we utilized the animal sample size estimation method proposed by Chen et al.[84] The calculation was performed using G*Power 3.1.9.7 (Universität Düsseldorf, Germany). The probability values for type I and type II errors were set at 0.05 and 0.20, respectively. The power analysis indicated that a minimum of 8 mice in each group was necessary.

Forty-eight six-week-old male C57BL/6 mice (with an average weight of 21.83 ± 1.19 g) were obtained from the Guangdong Medical Laboratory Animal Center and housed at the Shenzhen Peking University-Hong Kong University of Science and Technology (PKU-HKUST) Medical Center Animal Experiment Center. The mice were adaptively feeding for a week before being randomly divided into six equal groups (n = 8) using random number tables. All mice were housed in hygienic plastic cages within a clean and well-ventilated room, with free access to food and water. The room was maintained at a constant temperature of 21 ± 1°C and relative humidity ranging from 40% to 60%. The mice were subjected to 12-h light and dark cycles.

To design animal experiments for iron overload-induced osteoarthritis (IOOA), we consulted several previous studies and made necessary adjustments based on the specific circumstances.[20–22,32,85,86] The animals were divided into the following groups: (1) Sham group, (2) Destabilized Medial Meniscus (DMM) group (applied to the remaining groups), (3) DMM + iron dextran (ID) (I812123, Macklin, Shanghai, China) (IOOA) group (500 mg/kg/week administered intraperitoneally from 7 to 14 weeks old, applied to the remaining groups), (4) IOOA + RSG (R014317, Rhawn, Shanghai, China)-L group (0.1 mg/kg RSG (10 μL) administered by intra-articular injection from post-operative DMM at 9 weeks old, once a week for 8 consecutive weeks), (5) IOOA + RSG-M group (0.2 mg/kg RSG (10 μL) administered by intra-articular injection from post-operative DMM at 9 weeks old, once a week for 8 consecutive weeks), (6) IOOA + RSG-H group (0.3 mg/kg RSG (10 μL) administered

by intra-articular injection from post-operative DMM at 9 weeks old, once a week for 8 consecutive weeks). Under isoflurane anesthesia (R510-22, RWD Life Science, Shenzhen, China) administered in an anesthesia chamber, the mice underwent surgery on the right leg to induce the DMM model. For the Sham group, only the skin was incised to open the joint cavity, and the skin was sutured. Injections for the Sham, DMM, and IOOA groups were administered with an equal volume (10 μL) of sterile physiological saline once a week for eight consecutive weeks. After surgery, the mice were anesthetized and awakened, and fed and watered normally. Body weight of mice was monitored weekly.

At 17 weeks of age, the injection of ID was discontinued, murine biological samples were acquired. Following isoflurane anesthesia administration, mice were euthanized through cervical dislocation. Subsequent experiments involved the collection and processing of complete knee samples from all groups. The knee joint of the operated leg was separated, and the surrounding soft tissues were removed as cleanly as possible. Subsequently, the isolated knee joint was placed in 4% paraformaldehyde fixative tissue fixation fluid (G1101, Servicebio, Wuhan, China) for 48 h for fixation.

All animal procedures comply with the ARRIVE guidelines and adhere to the U.K. Animals (Scientific Procedures) Act, 1986, European guidelines (2010/63/EU), and the Regulations for the Administration of Affairs Concerning Experimental Animals approved by the State Council of the People's Republic of China. The study was approved by the Animal Ethics Committee of the Shenzhen Peking University-Hong Kong University of Science and Technology Medical Center (No. 2023-138).

METHOD DETAILS

Chondrocytes preparation and treatment

Primary mouse chondrocytes (CP-M087, Procell, Wuhan, China) were cultured in complete Dulbecco's Modified Eagle's Medium: Nutrient Mixture F-12 (DMEM/F12) at 37°C in a 5% CO_2 atmosphere. The first three passages were used for all experiments.

Rosiglitazone (RSG) (R014317, Rhawn, Shanghai, China) was dissolved in Dimethyl sulfoxide (DMSO) (D8371, Solarbio, Beijing, China) at a stock concentration of 200 mM and then diluted in DMEM/F12 complete medium at a series of concentrations (0, 12.5, 25, 50, 100, 200 μM). DMSO served as the drug vehicle, and its final concentration was no more than 0.1%.

After determining the optimal concentration of RSG, chondrocytes were seeded in 6-well plates at a density of 1×10^6 cells per well and allowed to adhere for 24 h to receive different treatments. The first group served as the control, and chondrocytes were treated with DMEM/F12 medium containing 0.1% DMSO throughout all experimental time points. In the second group, chondrocytes were treated with 10 ng/mL recombinant mouse Interleukin-1β (IL-1β) (211-11B, PeproTech, New Jersey, USA) alone for 24 h to induce OA-like inflammatory conditions. For the third group, chondrocytes were stimulated with 100 μM Ferric Ammonium Citrate (FAC) (R017760, Rhawn, Shanghai, China) alone for 24 h to induce an iron overload environment. In the fourth group, chondrocytes were treated with 10 ng/mL IL-1β for 24 h followed by the optimal concentration of RSG for an additional 24 h. For the fifth group, chondrocytes were stimulated with 100 μM FAC for 24 h followed by the optimal concentration of RSG for an additional 24 h.

Cell counting Kit-8 (CCK-8) assay

To examine the effect of RSG on cell viability, chondrocytes were treated with different concentrations (0, 12.5, 25, 50, 100, and 200 μM) of RSG. After 24 and 48 h of incubation at 37°C, 10 μL of the CCK-8 solution (C0037, Beyotime, Shanghai, China) was added to each well and incubated at 37°C in darkness for 2 h. The absorbance was measured at 450 nm using a microplate reader (Multiskan FC, Thermo Scientific, Massachusetts, USA). The optical density values were compared to evaluate the cell viability of the different groups.

Toluidine blue (TB) staining

To observe the morphology of chondrocytes, TB staining was applied. Operational steps are as follows: 1. Remove the original culture medium, wash twice with 1×PBS buffer (PB180327, Procell, Wuhan, China), each time for 1 min; 2. Add an appropriate amount of toluidine blue staining solution (for cells) (G3660, Solarbio, Beijing, China) to each well and stain for 5 min; 3. Add an equal amount of distilled water, gently shake the culture plate, and let it stand for 15 min; 4. Wash twice with distilled water, each time for 20 s, and inspect under a microscope after adding an appropriate amount of distilled water to completely submerge the cells. The morphological characteristics of chondrocytes were observed using a microscope (DMi8, Leica, Wetzlar, Germany).

5-Ethynyl-20-Deoxyuridine (EdU) staining assay

The EdU kit (C0075S, Beyotime, Shanghai, China) was employed to assess proliferation. The specific steps were carried out according to the kit instructions. Briefly, after being subjected to different treatments, the chondrocytes were incubated with the EdU solution for 2 h at 37°C, fixed with 4% paraformaldehyde (P0099, Beyotime, Shanghai, China) for 15 min, permeabilized with 0.3% Triton X-100 (T8200, Solarbio, Beijing, China) for 10 min, and rinsed with 1×PBS buffer three times. The cells were then incubated with the Click Reaction Mixture for 30 min at room temperature under protection from light. Nuclei were labeled with Hoechst 33342 Staining Solution (C1025, Beyotime, Shanghai, China) for 5 min. Images were captured using an inverted fluorescence microscope (DMi8, Leica, Wetzlar, Germany).

Live/dead cell staining

The cell viability was measured through the Calcein-AM/Propidium Iodide (PI) double staining kit (C542, Dojindo, Kumamoto, Japan). The experimental procedures were as follows: 1. Digest cells with 0.25% trypsin-EDTA (G4001, Servicebio, Wuhan, China); 2. Collect cells by

centrifugation (1,000 rpm, 3 min); 3. Discard the supernatant, add 1×PBS buffer to prepare a cell suspension ($10^5 \sim 10^6$ cells/mL); 4. Repeat steps 2 and 3 several times to eliminate esterase activity in the culture medium; 5. Mix 100 μL staining working solution with 200 μL cell suspension and culture at 37°C for 15 min. Images were captured using an inverted fluorescence microscope (DMi8, Leica, Wetzlar, Germany).

Apoptosis detection

Apoptosis was assessed by flow cytometry (FCM) using the Annexin V-FITC/PI apoptosis detection kit (AD10, Dojindo, Kumamoto, Japan). In brief, the approach involves the following steps: 1. Discard the medium from the culture plates and wash the cells twice with 1×PBS buffer; 2. Digest the cells using 0.25% trypsin without EDTA (G4002, Servicebio, Wuhan, China); 3. Transfer the cell suspension to centrifuge tubes with an appropriate amount of medium; 4. After centrifugation at 1,000 rpm for 3 min, discard the supernatant; 5. Centrifuge again at 1,000 rpm for 3 min after adding 1×PBS buffer, and discard the supernatant. Repeat this step once; 6. Add pre-prepared 1×Annexin V Binding Solution to make a final concentration of 1×10^6 cells/mL cell suspension; 7. Take 100 μL of the cell suspension from step 6 and add it to a new EP tube; 8. Add 5 μL Annexin V, FITC conjugate, and then add 5 μL PI solution to the cell suspension; 9. Incubate in the dark at room temperature for 15 min; 10. Add 400 μL 1×Annexin V Binding Solution. Subsequently, chondrocyte apoptosis was analyzed using the FCM (CytoFLEX S, Beckman Coulter, Brea, USA) and CytExpert (version 4.0, Beckman Coulter, Brea, USA).

Senescence-associated β-galactosidase (SA-β-Gal) staining assay

The SA-β-Gal staining assay was conducted according to the manufacturer's instructions (G1580, Solarbio, Beijing, China). The experiment procedures were shown as follows: 1. Remove the original cell culture medium, wash once with 1×PBS buffer, add 1 mL of β-Gal fixation solution, and fix at room temperature for 15 min; 2. Remove the cell fixation solution, wash the cells three times with 1×PBS buffer, each time for 3 min; 3. Prepare the staining working solution according to the proportion. Remove the β-Gal wash solution, and add 1 mL of staining working solution to each well; 4. Incubate at 37°C overnight (cover the 6-well plate with plastic wrap to prevent evaporation). Images were captured using a microscope (DMi8, Leica, Wetzlar, Germany).

Intracellular iron assay

The intracellular concentration of ferrous ions was determined using the ferrous ion content assay kit (BC5410, Solarbio, Beijing, China) and the Prussian blue iron stain kit for cells (G1426, Solarbio, Beijing, China), following the manufacturer's instructions. The brief experimental procedure for ferrous ion content assay kit is as follows: According to the cell number (10^4 cells): reaction reagent volume (mL) at a ratio of $500 \sim 1000:1$, sonicate cells on ice (power 200W, ultrasound 3 s, interval 7 s, total time 5 min); then centrifuge at 10,000g, 4°C for 10 min, collect the supernatant and keep it on ice for further analysis. Then, prepare the reaction systems required for each assay according to the instructions of the kit. Mix thoroughly, then centrifuge at 12,000 g at room temperature for 10 min. Carefully pipette 800 μL of the upper aqueous phase into a 1mL glass cuvette. Measure the absorbance at 593 nm using a microplate reader (Multiskan FC, Thermo Scientific, Massachusetts, USA), and then calculate the ferrous ion content further according to the instructions of the kit. The brief experimental procedure for the Prussian blue iron stain kit is as follows: Fix samples in 4% paraformaldehyde for $10 \sim 20$ min. Incubate the plate filled with prepared Perls' staining solution at 37°C for 30 min. Rinse twice with tap water, each time for 2 min. Apply Perls' reagent drops onto the plate, re-stain for 30 s. Stained cells were captured using a microscope (DMi8, Leica, Wetzlar, Germany).

Additionally, the concentrations of iron in the cytoplasm and mitochondria were evaluated using the FerroOrange (F374, Dojindo, Kumamoto, Japan) and Mito-FerroGreen (M489, Dojindo, Kumamoto, Japan) fluorescent probes. The brief experimental procedure for FerroOrange and Mito-FerroGreen is as follows: Discard the supernatant and wash the cells three times with serum-free DMEM/F12 medium (G4612, Servicebio, Wuhan, China); Add FerroOrange or Mito-FerroGreen working solution and incubate at 37°C with 5% CO_2 for 30 min. Fluorescence measurements were conducted using FCM (CytoFLEX S, Beckman Coulter, Brea, USA) and a fluorescent microscope (DMi8, Leica, Wetzlar, Germany).

Detection of reactive oxygen species (ROS) and lipid peroxidation

Intracellular ROS levels were assessed using the ROS assay kit (S0033S, Beyotime, Shanghai, China), and mitochondrial superoxide was analyzed with the mtSOX Deep Red mitochondrial superoxide detection kit (MT14, Dojindo, Kumamoto, Japan). Experiments were conducted following the kit instructions. The brief experimental procedure for ROS assay kit is as follows: Dilute DCFH-DA with serum-free DMEM/F12 medium at a ratio of 1:1000 to achieve a final concentration of 10 μmol/L. After cell collection, suspend the cells in the diluted DCFH-DA, with a cell concentration of one to twenty million/mL, and incubate at 37°C in a cell culture incubator for 20 min. Invert the mixture every 3 to 5 min to ensure full contact between the probe and the cells. Wash the cells three times with serum-free DMEM/F12 medium to thoroughly remove DCFH-DA that has not entered the cells. Fluorescence microscope (DMi8, Leica, Wetzlar, Germany) analysis and FCM (CytoFLEX S, Beckman Coulter, Brea, USA) were employed for cell examination. The brief experimental procedure for mtSOX Deep Red mitochondrial superoxide detection kit is as follows: Remove the culture medium and wash the cells with medium; Remove the supernatant, add the prepared mtSOX Deep Red working solution, and culture at 37°C, 5% CO_2 for 30 min; Wash the cells twice with 1×PBS buffer; Observe the cells under a fluorescence microscope (DMi8, Leica, Wetzlar, Germany).

Lipid peroxidation was measured using the malondialdehyde (MDA) assay kit (S0131S, Beyotime, Shanghai, China), C11 BODIPY[581/591] (L267, Dojindo, Kumamoto, Japan), and Liperfluo fluorescent probe (L248, Dojindo, Kumamoto, Japan). All experimental procedures adhered

to the kit specifications. The brief experimental procedure for MDA assay kit is as follows: cells were lysed with cell lysis buffer (P0013, Beyotime, Shanghai, China), and the protein concentration was measured using the bicinchoninic acid (BCA) protein assay kit (KGB2101, KeyGEN BioTECH, Nanjing, China) kit. Subsequently, 100 μL of cell lysates were incubated with 200 μL of MDA test solution at 100°C for 15 min. After centrifugation at 1,000×g for 10 min, 200 μL of supernatant was transferred to a 96-well plate, and absorbance was measured at 532 nm using a microplate reader (Multiskan FC, Thermo Scientific, Massachusetts, USA). The brief experimental procedure for C11 BODIPY[581/591] and Liperfluo kit is as follows: Remove the culture medium and wash the cells with medium; Remove the supernatant, add the prepared C11 BODIPY[581/591] and Liperfluo working solution, and culture at 37°C, 5% CO_2 for 30 min; Wash the cells twice with 1×PBS buffer. The fluorescence of the C11 BODIPY[581/591] and Liperfluo was subsequently quantified using FCM (CytoFLEX S, Beckman Coulter, Brea, USA) and an inverted fluorescence microscope (DMi8, Leica, Wetzlar, Germany).

Measurement of reduced glutathione (GSH) and oxidized glutathione Disulfide (GSSG)

The intracellular levels of GSH and GSSG, along with the GSH/GSSG ratio, were determined using the GSH and GSSG Assay kit (S0053, Beyotime, Shanghai, China) following the manufacturer's instructions. Briefly, GSSG was reduced to GSH by glutathione reductase, and then reacted with the chromogenic substrate DTNB to produce yellow TNB and GSSG. GSH was depleted by GSH scavenging auxiliary fluid before measuring GSSG using the aforementioned reaction principle. GSH levels were calculated by subtracting GSSG from the total glutathione (GSSG+GSH). The reaction mixture was dispensed into a 96-well plate, and the absorbance at 412 nm was measured using a microplate reader (Multiskan FC, Thermo Scientific, Massachusetts, USA).

Glutamine and glutamate assays

Glutamine and glutamate levels were determined using the glutamine assay kit (G0429W, Geruisi) and glutamate assay kit (BC1585, Solarbio, Beijing, China), respectively, in accordance with the manufacturer's instructions.

The brief experimental procedure for glutamine assay kit is as follows: First, collect cells into centrifuge tubes, discard the supernatant after centrifugation; take about 5 million cells and add to 1mL of extraction solution, sonicate bacteria or cells (on ice, power 200W, ultrasound 3 s, interval 10 s, repeat 30 times); centrifuge at 12,000rpm, 4°C for 10 min, collect the supernatant, and keep it on ice for further analysis. Then, prepare the reaction systems required for each assay according to the instructions of the kit. Mix thoroughly, then incubate at 37°C in a water bath for 30 min. Immediately after incubation, measure the absorbance at 450 nm wavelength using a microplate reader (Multiskan FC, Thermo Scientific, Massachusetts, USA) for each group. Finally, calculate the glutamine content according to the instructions provided with the kit.

The brief experimental procedure for glutamate assay kit is as follows: Cells are prepared according to cell number (10^6 cells): reaction reagent volume (mL) at a ratio of 5~1:1, cells are sonicated on ice (power 200W, ultrasound 3 s, interval 10 s, total time 3 min); centrifugation at 10,000rpm, 4°C for 10 min, collect the supernatant and keep it on ice for further analysis. Then, prepare the reaction systems required for each assay according to the instructions of the kit. Mix thoroughly, then incubate at 37°C for 30 min. Immediately measure the absorbance at 340 nm wavelength using a microplate reader (Multiskan FC, Thermo Scientific, Massachusetts, USA) for each group. Finally, calculate the glutamate content according to the instructions provided with the kit.

Superoxide dismutase (SOD) activity

SOD activity was assessed using the kit (BC5165, Solarbio, Beijing, China) following the provided instructions. The brief experimental procedure is as follows: Collect cells into centrifuge tubes, discard the supernatant after centrifugation, according to the number of bacteria or cells (10^4 cells): extraction volume (mL) = 500~1000:1 ratio (500 million cells added to 1mL extraction solution), sonicate the cells (on ice, power 200W, ultrasound 3 s, interval 10 s, repeat 30 times), centrifuge at 8,000g 4°C for 10 min, collect the supernatant, and keep it on ice for further analysis. Then, prepare the reaction systems required for each assay according to the instructions of the kit. Mix the samples thoroughly, incubate them at 37°C for 30 min in a water bath, and measure the absorbance at 450 nm using a microplate reader (Multiskan FC, Thermo Scientific, Massachusetts, USA). Then further calculate the activity of SOD in cells according to the instructions of the kit.

Mitochondrial membrane potential

The mitochondrial membrane potential was evaluated through Rhodamine 123 staining (C2008S, Beyotime, Shanghai, China) and JC-1 probe (C2006, Beyotime, Shanghai, China). The brief experimental procedure for Rhodamine 123 is as follows: 1. Digest cells using 0.25% trypsin-EDTA (G4001, Servicebio, Wuhan, China) and count; 2. Centrifuge an appropriate amount of cells at 600×g for 5 min at room temperature, discard the supernatant, add an appropriate volume of Rhodamine 123 staining working solution to resuspend the cells, achieving a cell density of approximately 1×10^6 cells/mL; 3. Incubate at 37°C in a cell culture incubator for 30 min; 4. After incubation at 37°C, centrifuge at 600×g for 5 min at room temperature, pellet the cells, and remove the supernatant; 5. Wash twice with pre-warmed cell culture medium at 37°C: add 1 mL of pre-warmed cell culture medium at 37°C to resuspend the cells, centrifuge at 600×g for 5 min, pellet the cells, and discard the supernatant; repeat this step once; 6. Resuspend the cells in an appropriate amount of cell culture medium, observe under an inverted fluorescence microscope (DMi8, Leica, Wetzlar, Germany), or analyze by FCM (CytoFLEX S, Beckman Coulter, Brea, USA).

The brief experimental procedure for JC-1 is as follows: 1. Digest cells using 0.25% trypsin-EDTA (G4001, Servicebio, Wuhan, China) and count; 2. Take 10~60 thousand cells and resuspend in 0.5mL of cell culture medium; 3. Add 0.5mL of JC-1 staining working solution, invert

several times to mix. Incubate at 37°C in a cell culture incubator for 20 min; 4. During the incubation period, prepare an appropriate amount of JC-1 staining buffer (1X) by adding 4mL of distilled water to every 1mL of JC-1 staining buffer (5X), and place it on ice; 5. After incubation at 37°C, centrifuge at 600×g at 4°C for 34 min, pellet the cells, and discard the supernatant; 6. Wash twice with JC-1 staining buffer (1X): add 1mL of JC-1 staining buffer (1X) to resuspend the cells, centrifuge at 600×g at 4°C for 3~4 min, pellet the cells, and discard the supernatant. Repeat this step once; 7. Resuspend the cells in an appropriate amount of JC-1 staining buffer (1X), and analyze by FCM (CytoFLEX S, Beckman Coulter, Brea, USA).

Fluorescence staining of the membrane-containing organelles

To estimate cellular organellar mass, cells were stained with organelle-specific fluorescence dyes: Mito-Tracker Green (C1048, Beyotime, Shanghai, China), LysoTracker red (C1046, Beyotime, Shanghai, China), ER-Tracker Green (C1042S, Beyotime, Shanghai, China), and Golgi-Tracker Red (C1043, Beyotime, Shanghai, China), following the manufacturer's instructions. Brief experimental procedures are as follows: Remove the original cell culture medium, add pre-prepared Mito-Tracker Green, LysoTracker red, ER-Tracker Green, or Golgi-Tracker Red staining working solution according to the instructions, and co-incubate with cells at 37°C for 15~45 min. Then remove the staining working solution, and wash the cells 1~2 times with fresh cell culture medium. Fluorescence was quantified using an inverted fluorescence microscope (DMi8, Leica, Wetzlar, Germany) and FCM (CytoFLEX S, Beckman Coulter, Brea, USA).

Transmission electron microscope (TEM)

Chondrocytes were trypsinized, centrifuged, and then fixed overnight at 4°C, protected from light, with 2.5% Glutaraldehyde (G1102, Servicebio, Wuhan, China). Following this, chondrocytes were washed with 1×PBS buffer and fixed with 1% osmium tetroxide for 1 h. Subsequently, the specimens underwent dehydration through a series of ethanol concentrations (30%, 50%, 70%, 80%, 95%, 100%) and 100% acetone. Finally, the samples were embedded, sectioned, and stained with uranyl acetate and lead citrate. A TEM (HT7700, Hitachi, Tokyo, Japan) was employed to visualize mitochondria morphology within chondrocytes.

Quantitative Real-time PCR (qPCR)

Total ribonucleic acid (RNA) from chondrocytes was extracted using the total RNA isolation kit (082001, Beibei Biotechnology, Zhengzhou, China) and quantified with the NanoDrop One nucleic acid protein detector (Thermo Scientific, Massachusetts, USA). Complementary cDNA was synthesized through reverse transcription with the PrimeScript RT reagent kit with gDNA Eraser (RR047A, Takara, Kyoto, Japan). The qPCR was conducted using TB Green Premix DimerEraser (RR091A, Takara, Kyoto, Japan) on the LightCycler 480 qPCR System (Roche, Basel, Switzerland). Gene expression levels were normalized to GAPDH. The relative expression levels of RNA were calculated using the $2^{-\Delta\Delta Ct}$ method.

Primers were obtained from Sangon (Shanghai, China), and their sequences are provided in Table S1.

Protein extraction and Western Blot

After being washed twice with precooled 4°C 1×PBS buffer, total proteins from chondrocytes subjected to various treatments were extracted using RIPA lysis buffer (G2033, Servicebio, Wuhan, China) containing PMSF (G2008, Servicebio, Wuhan, China). The protein concentration was measured using the BCA protein assay kit. The obtained proteins (3.5 μg/μL) were separated by 10% SDS-PAGE (WB1102, Biotides, Bejing, China) in running buffer (G2144, Servicebio, Wuhan, China) and then transferred onto 0.2 μm PVDF membranes (ISEQ00010, Millipore, Massachusetts, USA) using the trans-buffer (G2145, Servicebio, Wuhan, China) at 330 milliamperes (mA) for 90 min. Afterward, the membranes were blocked with 5% skim milk in 1×TBST buffer (G2150, Servicebio, Wuhan, China) for 1 h at room temperature. The membranes were incubated overnight at 4°C with the primary antibodies and then washed with 1×TBST buffer 3 times (10 min each time), followed by incubation with HRP-labeled goat anti-rabbit IgG secondary antibody (AS014, ABclonal, Wuhan, China) for 1 h at room temperature. After rinsing 3 times in 1×TBST buffer for 10 min, the bands of interest were visualized with the super-sensitive ECL chemiluminescent substrate (BL520B, Biosharp, Hefei, China), and a luminescent image analyzer (Amersham ImageQuant 800, Buckinghamshire, UK). Antibodies against GAPDH (5174S, Cell Signaling Technology, Massachusetts, USA) and Vinculin (FNab09799, FineTest, Wuhan, China) served as control for protein loading. GAPDH antibodies were used at a 10,000-fold dilution, Vinculin antibodies were used at a 2,000-fold dilution, and other antibodies were used at a 1,000-fold dilution. The secondary antibody was diluted in the blocking solution at a 1:10,000 dilution.

Enzyme-linked immunosorbent assay (ELISA)

ELISA was carried out following the instructions of two manufacturers (ABclonal and FineTest). The specific steps were as described in the ELISA kit.

Immunofluorescence (IF)

The cells were fixed in 4% paraformaldehyde for 15 min and permeabilized with 0.5% Triton X-100 (GC204003, Servicebio, Wuhan, China) for 15 min at room temperature. Then, they were blocked with 5% bovine serum albumin for 0.5 h at room temperature and incubated overnight with anti-ACSL4 (A20414, ABclonal, Wuhan, China) primary antibodies, anti-GPx4 (FNab03622, FineTest, Wuhan, China) primary antibodies, and anti-TfR1 (FNab08931, FineTest, Wuhan, China) primary antibodies at 4°C with gentle shaking. After being washed three

times with 1×PBS buffer for 10 min, the cells were exposed to fluorescence secondary antibodies (AS011, ABclonal, Wuhan, China) or (4413S, Cell Signaling Technology, Massachusetts, USA). The nuclei were counter-labeled with 2-(4-Amidinophenyl)-6-indolecarbamidine dihydrochloride (DAPI) (C1005, Beyotime, Shanghai, China). IF images were displayed on an inverted fluorescence microscope (DMi8, Leica, Wetzlar, Germany). All antibodies were used at a dilution of 1:200.

ACSL4 small interfering RNA (siRNA) transfection

GenePharma (Shanghai, China) chemically synthesized siRNA targeting the mouse ACSL4 gene and transfected it into chondrocytes. The sense sequence (5′→3′) of the ACSL4 siRNA was CCUGUCCACUUGUUAAUAATT, and its complementary antisense sequence (5′→3′) was UUAUUAACAAGUGGACAGGTT. Chondrocytes were seeded at a density of 1×10^6 cells/mL in 6-well plates and cultured until cells reached 60%~70% confluence. Following removal of the original cell culture medium, chondrocytes were incubated with serum-free DMEM/F12 medium containing si-ACSL4. The group of chondrocytes transfected with an empty vector was used as the negative control. si-ACSL4 was transiently transfected into chondrocytes using GP-transfect-Mate (G04009, GenePharma, Shanghai, China), and the medium was replaced 24 h after transfection.

Glucose content detection

Glucose assay kit with O-toluidine (S0201S, Beyotime, Shanghai, China) was used to detect glucose content. The experimental procedures were as follows: Remove the culture medium and wash twice with an appropriate amount of PBS. Add 100~200 µL of cell and tissue lysis buffer for glucose assay (S3062, Beyotime, Shanghai, China) per well of a 6-well plate (approximately 1×10^6 cells/well). Mix by pipetting for full lysis and centrifuge at 12,000×g for 5 min. Take the supernatant for glucose measurement. Add 5 µL of sample or standard to PCR tubes. Add glucose assay reagent to a final volume of 190 µL. Mix by vortexing and briefly centrifuge to allow liquid to accumulate at the bottom of PCR tubes. Place the tubes in a thermal cycler. Heat at 95°C for 8 min and then cool down to 4°C. Transfer 180 µL of reaction mixture per tube to a clear 96-well plate. Measure the absorbance at OD 630 nm using a microplate reader (Multiskan FC, Thermo Scientific, Massachusetts, USA). Calculate the glucose concentration in the sample based on the standard curve.

Molecular docking

The predicted structures of ACSL4 were generated using AlphaFold (https://alphafold.com/). The protonation state of all compounds was set at pH 7.4, and the compounds were expanded to 3D structures using Open Babel.[87] AutoDock Tools (ADT3) were employed to prepare and parameterize the receptor protein and ligands. Docking grid documents were generated by AutoGrid or Sitemap, and AutoDock Vina (1.2.0) was used for docking simulations.[88,89] The optimal pose was selected for analysis of the interaction. Finally, the protein-ligand interaction figure was generated using PyMOL (https://pymol.org/).

Micro-computed tomography (micro-CT)

The knee specimens of the mice were fixed in 4% paraformaldehyde fixative tissue fixation fluid and scanned using a micro-CT scanner (vivaCT 80, SCANCO MEDICAL, Switzerland) with a voxel size of 10.4 µm. The energy/intensity was set at 55 kV, 145 µA, and 8 W. Image data were reconstructed and processed using DataViewer, CTVox, and CTAn software (Bruker Biospin, Karlsruhe, Germany, Germany).

Histological staining

The collected knee specimens were fixed in 4% paraformaldehyde fixative tissue fixation fluid. Subsequently, the knees underwent decalcification in ethylenediaminetetraacetic acid decalcification fluid (G1105, Servicebio, Wuhan, China) using a shaker (37°C, 70 rpm) for one week. Following gradient dehydration, the knees were embedded in paraffin and sectioned along the coronal plane at 4 µm for subsequent histological staining. Staining procedures included Hematoxylin-Eosin (H&E) Stain Solution (G1005, Servicebio, Wuhan, China), TB Cartilage Stain Solution (G1032, Servicebio, Wuhan, China), and Saffron-O and Fast Green (SOFG) Stain Solution (G1053, Servicebio, Wuhan, China). Two independent evaluators, blinded to the treatment conditions, graded knee joint histopathology using the modified Mankin and Osteoarthritis Research Society International (OARSI) scoring systems.[90,91] Cartilage thickness was measured by width calculation, while the area of special-stained regions was determined using an area-calculating algorithm with ImageJ/Fiji 2.9.0 (National Institutes of Health, Bethesda, USA) (National Institutes of Health).

Immunohistochemical (IHC) staining

The processing methods for the collected knee specimens were the same as described above, followed by IHC staining. Paraffin sections were routinely deparaffinized (G1128, Servicebio, Wuhan, China), rehydrated, and repaired using a pepsin antigen repair solution (G0142, Servicebio, Wuhan, China) at 37°C for half an hour. The IHC evaluation procedure followed the instructions of the Ultra-Sensitive TM SP (Mouse/Rabbit) IHC Kit (KIT-9710, MXB Biotechnologies, Fuzhou, China). Additionally, the sections were incubated with MMP3 (FNab05244, FineTest, Wuhan, China), ADAMTS5 (bs-3573R, Bioss, Beijing, China), COX-2 (A1253, ABclonal, Wuhan, China), GPx4 (FNab03622, FineTest, Wuhan, China), ACSL4 (A20414, ABclonal, Wuhan, China), 4-HNE (bs-6313R, Bioss, Beijing, China), TfR1 (FNab08931, FineTest, Wuhan, China), and Nrf2 (GB113808-100, Servicebio, Wuhan, China) at 4°C overnight in the dark. On the next day, the HRP-labeled goat anti-rabbit IgG secondary antibody (AS014, ABclonal, Wuhan, China) was applied, and the brown color was developed

using DAB staining (G1212, Servicebio, Wuhan, China). Nrf2 antibodies were used with a 1,000-fold dilution and other antibodies were used with a 200-fold dilution. The stained slices were captured with a microscope (DM4B, Leica, Wetzlar, Germany), and the positive areas in the representative images were statistically summarized using ImageJ/Fiji 2.9.0 (National Institutes of Health, Bethesda, USA).

In vivo biosafety assessment of RSG intra-articular injection

For the biotoxicity study, twelve six-week-old male C57BL/6 mice were randomly divided into four groups ($n = 3$ per group) using random number tables. The control group received intra-articular injections of PBS (10 μL) once a week for eight consecutive weeks. The remaining three groups received intra-articular injections of RSG solution at three different concentrations (low, medium, and high: 0.1/0.2/0.3 mg/kg, 10 μL each) once a week for eight consecutive weeks. Animal housing conditions were as described previously. After the eight-week experimental period, injections were discontinued, and murine biological samples were collected. After administering isoflurane anesthesia, blood was collected via eyeball removal for routine blood tests (BC-2800 Vet, Mindray, Shenzhen, China), as well as for hepatic and renal function tests, including glutamic-pyruvic transaminase, glutamic-oxalacetic transaminase, urea nitrogen, and serum creatinine (Chemray 800, Rayto, Shenzhen, China). The mice were euthanized via cervical dislocation under isoflurane-induced general anesthesia. The main organs, including the heart, liver, spleen, lungs, and kidneys, were dissected for histological staining. Tissue processing and staining were performed as described previously.

QUANTIFICATION AND STATISTICAL ANALYSIS

The data were compiled and independently analyzed by two authors (SYC and YHW). GraphPad Prism 9.5 (GraphPad Software, San Diego, USA) was used for all analyses. Quantitative data represent the results of at least three independent experiments, and only data from a representative experiment are presented. Pairwise comparisons were performed using Student's *t*-tests, while multi-group comparisons were conducted using one-way analysis of variance (ANOVA). Data are presented as mean $\pm$ standard deviation. Two-tailed p values were calculated, and statistical significance was defined as $p < 0.05$, denoted as 'ns' for no statistical difference, and indicated as $*p < 0.05$, $**p < 0.01$, $***p < 0.001$.